



Automatic superpixel-based segmentation method for breast ultrasound images



Mohammad I. Daoud^{a,*}, Ayman A. Atallah^a, Falah Awwad^b, Mahasen Al-Najjar^c, Rami Alazrai^a

^aDepartment of Computer Engineering, German Jordanian University, Amman-Madaba Street, Amman, Jordan

^bDepartment of Electrical Engineering, United Arab Emirates University, Sheikh Khalifa Bin Zayed Street, Al-Ain, United Arab Emirates

^cDepartment of Radiology, The University of Jordan, Queen Rania Street, Amman, Jordan

ARTICLE INFO

Article history:

Received 28 May 2018

Revised 27 October 2018

Accepted 13 November 2018

Available online 22 November 2018

Keywords:

Ultrasound breast images

Superpixels

Graph cuts segmentation

Active contour models

Support vector machine

Breast cancer diagnosis

ABSTRACT

Automatic and accurate breast ultrasound (BUS) image segmentation is crucial to achieve effective ultrasound-based computer aided diagnosis (CAD) systems for breast cancer. However, segmenting the tumor in BUS images is often challenging due to several artifacts that degrade the quality of ultrasound images. In this study, a new two-phase method is proposed to enable automatic and accurate segmentation of BUS images by decomposing the image into superpixels with high boundary recall ratio and employing edge- and region-based information to outline the tumor. The first phase of the method obtains an initial outline of the tumor by decomposing the BUS image into coarse superpixels to enable effective estimation of their tumor likelihoods and employing a customized graph cuts algorithm to segment the superpixels. The segmentation of the superpixels is carried out using edge-based information that quantifies the image contour cue and region-based information that characterizes the texture content of the superpixels. In the second phase, the tumor outline is improved by decomposing the BUS image into fine superpixels that enable high boundary recall ratio and employing the customized graph cuts algorithm to segment the superpixel located around the initial tumor outline. Furthermore, an edge-based active contour model is used to smooth the tumor outline. The performance of the proposed method was evaluated using a database that includes 160 BUS images (86 benign and 74 malignant). The results indicate that the first phase of the proposed method was able to detect the tumor in all BUS images and obtain mean values of the true positive ratio (TPR), false positive ratio (FPR), false negative ratio (FNR), similarity ratio (SIR), Hausdorff error (HE), and mean absolute error (ME) equal to 91.68, 11.16, 8.32, 84.52, 17.59, and 4.67, respectively. In fact, the results obtained by the first phase of the proposed method outperform four existing BUS image segmentation algorithms. Moreover, the second phase of the proposed method was able to improve the tumor outlines of the first phase and achieve mean TPR, FPR, FNR, SIR, HE, and ME values of 96.04, 7.99, 3.96, 91.41, 11.66, and 3.65, respectively. These results suggest the feasibility of employing the proposed method, which enables automatic and accurate tumor segmentation in BUS images, to develop effective CAD systems for breast cancer.

© 2018 Elsevier Ltd. All rights reserved.

1. Introduction

Breast cancer is one of the most prevalent malignancies in females and the fifth most frequent cause of cancer-related deaths in the world (Ferlay et al., 2015). In 2012, 522,000 deaths were related to breast cancer and 1.67 million women were diagnosed with the disease (Ferlay et al., 2015). Early detection of breast can-

cer is important for reducing the associated mortality rates and achieving effective treatment of the disease (Kaul & Daguilh, 2002).

Mammography is the most common imaging modality for diagnosing breast cancer (Schulz-Wendtland, Fuchsberger, Wacker, & Hermann, 2009). However, mammography has some limitations, such as the reduced sensitivity of detecting breast cancer in women with dense breast (Kelly, Dean, & Lee, 2010; Kolb, Lichy, & Newhouse, 2002). Ultrasound imaging is an important adjunct to mammography for improving breast cancer diagnosis (Nothacker et al., 2009). It offers the advantages of low cost, safety, and real-time imaging capability. Combining ultrasound imaging of the breast with mammography can detect cancerous tumors not

* Corresponding author.

E-mail addresses: mohammad.aldaoud@gju.edu.jo (M.I. Daoud), ayman.atallah@gju.edu.jo (A.A. Atallah), f_awwad@uaeu.ac.ae (F. Awwad), m.najar@ju.edu.jo (M. Al-Najjar), rami.azrai@gju.edu.jo (R. Alazrai).

seen on mammography alone (Nothacker et al., 2009). For women with dense breast, ultrasound achieves higher sensitivity than mammography for detecting breast abnormalities (Leconte et al., 2003). Moreover, ultrasound texture analysis can be used to substantially minimize the number of breast biopsies performed for benign tumors (Garra et al., 1993). Furthermore, the rate of detecting breast cancer using ultrasound is suggested to be comparable with mammography (Berg et al., 2016).

Breast cancer diagnosis using ultrasound imaging is operator-dependent, and hence experienced radiologists are required to interpret breast ultrasound (BUS) images. Moreover, the interpretation of BUS images by experienced radiologists might have some inter-observer variability (Calas, Almeida, Gutfilen, & Pereira, 2010; Timmers, van Doorn-Nagtegaal, Verbeek, & den Heeten, 2012). To address these limitations, several studies, such as Rouhi, Jafari, Kasaei, and Keshavarzian (2015), Daoud, Bdair, Al-Najar, and Alazrai (2016b), and Singh, Verma, and Thoke (2016), proposed computer-aided diagnosis (CAD) systems to interpret BUS images using computational analyses of the image characteristics. These systems aim to provide a second opinion to the radiologist with the goal of achieving breast cancer diagnosis with high accuracy and subjectivity (Cheng, Shan, Ju, Guo, & Zhang, 2010a; Huang, Luo, & Zhang, 2017). Many features that are employed by CAD systems for differentiating benign and malignant breast tumors are based on the shape and texture of the tumor (Cheng et al., 2010a; Daoud et al., 2016b; Zakeri, Behnam, & Ahmadinejad, 2012). Hence, accurate segmentation of BUS images is essential to achieve effective CAD systems that minimize the operator dependency and improve the reproducibility of the diagnosis process. Due to its importance, BUS image segmentation is considered in this study.

Manual segmentation of BUS images involves several limitations, such as the long processing time and substantial operator dependency. Therefore, developing computer-based methods for segmenting BUS images is crucial to achieve automated and reliable CAD systems. However, the task of developing computer-based segmentation methods is considered challenging due to several inherent artifacts that degrade the quality of BUS images (Cheng et al., 2010a; Huang et al., 2017). Examples of these artifacts include ultrasound speckle (de Araujo, Constantinou, & Tavares, 2016), acoustic shadowing (Kirberger, 1995), and low contrast (Chang, Wu, Moon, & Chen, 2003). Furthermore, the presence of tumor-like structures in the BUS image, such as fat and acoustic shadowing, and the substantial variations in the sizes and shapes of breast tumors increase the complexity of the segmentation task (Liu et al., 2009; Madabhushi & Metaxas, 2003; Xie, Chen, & Lin, 2017).

In general, computer-based BUS image segmentation methods can be classified as semi-automatic methods and fully automatic methods (Gomez-Flores & Ruiz-Ortega, 2016; Huang et al., 2017; Xian et al., 2018). In semi-automatic methods, the tumor segmentation process involves user interaction, where the user is asked to identify a region in the BUS image that includes the tumor, a seed point inside the tumor, or an initial outline of the tumor. Then, the manually-selected tumor region, tumor seed point, or initially tumor outline is refined using computer-based algorithms to determine the tumor boundary. On the other hand, fully automatic BUS image segmentation methods do not require any user interaction, and hence the identification of the location of the tumor in the BUS image and the outlining of the tumor boundary are carried out using computer-based algorithms. The user-interaction requirement of the semi-automatic BUS image segmentation methods limits the complete automation and operator-independence of CAD systems. Hence, fully automatic methods are usually preferred (Xian, Zhang, & Cheng, 2015).

In the past few years, a large number of methods have been proposed for BUS image segmentation. Detailed review

of these methods is provided in Cheng et al. (2010a) and Huang et al. (2017). Commonly used methods include watershed algorithms, machine learning, active contour models, and graph-based algorithms. For example, Gomez, Leija, Alvarenga, Infantosi, and Pereira (2010) proposed a semi-automatic watershed method to outline the tumor in BUS images. In this method, a marker-controlled watershed transformation has been combined with an average radial derivative function. Cheng et al. (2010b) have also used watershed transformation to develop a semi-automatic tumor segmentation algorithm that integrates cell competition and cell-based contour grouping. In general, watershed algorithms suffer from the oversegmentation problem. The techniques that have been proposed to prevent the oversegmentation effect, such as the marker-controlled watershed (Gomez et al., 2010) and cell competition (Cheng et al., 2010b), might not completely overcome this problem (Shan, Cheng, & Wang, 2012).

Machine learning methods have been widely applied for segmenting BUS images. In general, these methods transform the BUS image segmentation problem into a classification problem. Shan et al. (2012) employed this approach to develop a fully automatic segmentation method in which a seed point is generated in the BUS image followed by the application of a region growing algorithm to select a ROI around the tumor. A neural network classifier was applied to classify each pixel in the ROI as lesion or background based on a set of multi-domain features. In a recent study, Rodrigues, Braz, Pereira, Moutinho, and Pinheiro (2015) introduced an automatic, two-stage method for segmenting BUS images. In the first step, an initial segmentation of the tumor is obtained using a support vector machine (SVM) classifier or discriminant analysis based on a pixel descriptor that includes multiresolution features computed using non-linear diffusion, bandpass filtering, and scale-variant mean curvature analyses. Heuristic operations are applied to post-process the initial segmentation. In the second stage, the initial segmentation is refined using an AdaBoost classification algorithm or active contours. The segmentation results obtained using this two-stage method suggested promising performance.

Other researchers employed active contour models to segment BUS images. For example, Lotfollahi, City, Ye, and Far (2017) proposed a semi-automatic, region-based active contour model to outline breast tumors in ultrasound images. The active contour model is used to iteratively evolve an initial contour, which is defined by the user, based on image intensity and a neutrosophic feature. In another study, Wang et al. (2014) developed a multi-scale segmentation method based on geodesic active contours. The method, which is applied to BUS images, is carried out from coarse scales to fine scales to enable effective capturing of the boundaries. Daoud, Baba, Awwad, Al-Najar, and Tarawneh (2012) introduced a semi-automatic active contour model that asks the user to define an initial circular contour inside the tumor. The vertices of the initial contour are iteratively moved towards the tumor boundary, such that their movements are controlled using a statistical parameter computed using ultrasound signal-to-noise ratio analysis. Despite the fact that active contour models can achieve good segmentation results, their performance is generally affected by some limitations such as the convergence to local optimal solutions and the high sensitivity to the initial contour (Rodrigues et al., 2015).

Recently, an increasing number of BUS image segmentation methods are developed based on the graph-based approach, which offers several advantages such as the simple construction and ability to incorporate various constraints to control the segmentation (Huang et al., 2017). Generally, the image pixels are represented in this approach as a weighted graph, where a node corresponds to a pixel or a set of pixels and an edge represents the similarity between two neighboring nodes. Image segmentation is obtained by partitioning the graph into groups, such that the similarities within the groups are maximized and the similarities between dif-

ferent groups are minimized. The graph-based approach has been employed by Xian et al. (2015), who proposed a fully automatic method that includes a ROI generation phase and a tumor segmentation phase. The first phase employs an adaptive reference point generation and a multipath search to localize a region in the BUS image that includes the tumor. In the second phase, the tumor is segmented using a graph-based framework that incorporates region- and edge-based features computed in the time and frequency domains. Another example is the study by Gao et al. (2012), in which a semi-automatic BUS image segmentation method is developed based on the normalized cuts (NCuts) framework (Shi & Malik, 2000). In this method, the local texture patterns in the BUS image are quantified by convolving the BUS image with a group of oriented filters and extracting a vector of texture features for each pixel in the BUS image. For a given BUS image, the extracted texture feature vectors are clustered into a finite number of feature vector groups using K-means clustering, where each feature vector group is called texton. Moreover, a boundary map is computed for the BUS image using boundary analyses that quantify the distributions of textons and the changes in pixels intensities. The boundary map is employed to define an adaptive neighborhood, called homogeneous patch, that includes neighboring pixels with similar characteristics. The distributions of textons within the homogeneous patches are analyzed to compute the final features that are processed by the NCut framework to segment the BUS image.

Despite the increasing number of segmentation methods that have been proposed in the literature, the task of achieving automatic and accurate outlining of the tumor in BUS images remains challenging. In particular, many of the previous segmentation methods, such as Lotfollahi et al. (2017) and Gao et al. (2012), are not fully automatic and require manual interaction. The similar characteristics between the tumor and other tumor-like structures, the irregular tumor shape, the heterogeneous texture patterns inside the tumor, and the blurred tumor boundary impose limitations on the ability of the segmentation methods to automatically and accurately segment the tumor.

The current study aims to propose a new segmentation method that combines edge- and region-based information to enable automatic and accurate segmentation of BUS images. Our approach is based on the decomposition of the BUS image into superpixels and the use of these superpixels to segment the image. The use of superpixels, instead of individual pixels, to carry out the segmentation provides several advantages, including the computational efficiency (Achanta et al., 2012) and the robustness to noise (Helala & Qureshi, 2014). Moreover, the use of superpixels enables effective local texture analysis due to the fact that they represent homogeneous subregions in the image with relatively large sizes (Zhang et al., 2016). In fact, various superpixel decomposition algorithms have been proposed in the literature, such as the quick shift (Vedaldi & Soatto, 2008), the NCuts algorithm (Shi & Malik, 2000), and the simple linear iterative clustering (SLIC) (Achanta et al., 2012). Among these algorithms, the SLIC algorithm provides an attractive image decomposing approach due to its low computational complexity and reduced memory requirements (Achanta et al., 2012). The use of superpixels for segmenting BUS images has been employed by recent studies (Daoud, Atallah, Awwad, & Al-Najjar, 2016a; Xi et al., 2017), which confirms the feasibility of this segmentation approach. The preliminary superpixel-based segmentation method that was proposed by our group (Daoud et al., 2016a) employed the NCuts algorithm to decompose the BUS image into 50 superpixels and used a simplified region growing procedure to analyze the superpixels and outline the tumor. The study by Xi et al. (2017) used the SLIC algorithm to decompose the BUS image into 500 superpixels and employed knowledge learning and level set segmentation to outline the tumor. In fact, the conventional superpixel decomposition algorithms, including the NCuts

and SLIC algorithms, are not specifically designed to generate superpixels that adhere well to the tumor boundary in BUS images. Such limitation might reduce the capability of achieving accurate segmentation of the tumor. To address this limitation, we have extended the SLIC algorithm to incorporate image contour cue during the decomposition process. Moreover, we have studied the effect of varying the number of generated superpixels on the boundary recall ratio and the ability of classifying the superpixels as tumor and background tissue. In fact, the boundary recall ratio is a metric that quantifies the percentage of the true tumor boundary that falls within a specific distance from the boundary of one of the generated superpixels (Achanta et al., 2012). Our analyses indicate that decomposing the BUS image into a small number of large superpixels enables effective estimation of their tumor likelihoods. Such a capability is crucial to detect the tumor in the BUS image. In addition, decomposing the BUS image into a large number of fine superpixels achieves high boundary recall ratio, which is important to achieve accurate tumor segmentation.

Based on these findings, we have developed a two-phase method that incorporates both region- and boundary-based information to segment BUS images. In the first phase, the BUS image is decomposed into a small number of coarse superpixels. The posterior tumor likelihood of each superpixel is estimated by extracting texture features from the superpixel and analyzing these features using a SVM classifier. An initial outline of the tumor is obtained by segmenting the superpixels using a customized graph cuts algorithm that incorporates both the image contour cue and the posterior tumor likelihoods of the superpixels. The parameters of the graph cuts algorithm are tuned using an automated grid search approach. The second phase is focused on refining the initial tumor outline obtained by the first phase to improve its accuracy. In particular, the BUS image is decomposed into a large number of fine superpixels to obtain high boundary recall ratio. Similar to the first phase, the posterior tumor likelihoods of the superpixels are computed using a SVM classifier. The superpixels are processed using a modified version of our customized graph cuts algorithm that restricts the segmentation to the local region around the initial tumor outline. Finally, the tumor outline is smoothed using an edge-based active contour model. The performance of our proposed method was evaluated by applying each phase to segment the tumors in a clinical BUS images database. We also have compared the performance of each phase of our proposed method with four well-studied BUS image segmentation methods that are introduced by Xian et al. (2015), Shan et al. (2012), Xi et al. (2017), and Gao et al. (2012). The performance comparisons are carried out in terms of the ability of detecting the tumor, area and boundary error metrics that evaluate the tumor segmentation, and an execution time metric. The main contributions of the paper can be summarized as follows:

- The development of an extended version of the SLIC algorithm that enables the decomposition of the BUS image into superpixels with high boundary recall ratios. Moreover, we have studied the effect of varying the number of superpixels on the boundary recall ratio of the superpixels and the ability of classifying the superpixels as tumor or background tissue.
- The development of a two-phase, superpixel-based method that supports automatic and accurate segmentation of BUS images. The first phase of the method aims to obtain an initial tumor outline by decomposing the BUS image into coarse superpixels and analyzing the superpixels using a customized graph cuts algorithm that incorporates both region- and boundary-based information. The second phase of the method aims to refine the tumor outline by decomposing the BUS image into fine superpixels, segmenting the superpixels using a customized version

of the graph cuts algorithm, and smoothing the tumor outline using an edge-based active contour model.

The remainder of the paper is organized as follows. **Section 2** describes the BUS image database and the extended SLIC algorithm that we have employed to decompose the BUS images into superpixels with high boundary recall ratios. Moreover, **Section 2** provides an overview of our proposed two-phase segmentation method, detailed descriptions of the two phases of the proposed method, and the performance analyses used to evaluate the proposed method. The experimental results are presented in **Section 3**. Finally, the discussion and conclusion are provided in **Sections 4** and **5**, respectively.

2. Materials and methods

In this section, the clinical BUS images database, which was used to evaluate the performance of the proposed method, is described. Furthermore, the extended SLIC algorithm, which is employed to obtain superpixels with high boundary recall ratios, is presented. We also have analyzed the effect of varying the number of superpixels on the boundary recall ratio of the superpixels and the ability of classifying the superpixels. Based on these analyses, the two-phase architecture of our proposed segmentation method is introduced, in which different numbers of superpixels are employed in each phase. Moreover, detailed description is provided for each phase of the proposed segmentation method. Finally, the procedures employed to evaluate the performance of the proposed method are summarized.

2.1. Data acquisition

The database employed in this study is composed of 160 BUS images. Among these images, there are 86 benign and 74 malignant cases, where all cases were identified as benign or malignant based on biopsy findings. The images were collected from August 2015 to January 2017 at the Jordan University Hospital, Amman, Jordan. The mean \pm standard deviation age of the patients was 48.2 ± 11.7 years. For each patient participated in the study, one BUS images was included in the database. Moreover, every BUS image contained one breast tumor and each image was captured at the largest tumor diameter. The acquisition of the BUS images was performed using an Acuson S2000 ultrasound imaging system (Siemens AG, Munich, Germany) equipped with a 5–14 MHz linear transducer. The radiologist was free to control the imaging parameters, such as the depth, focal length, and gain, to achieve the best view. The size of the acquired BUS images along the lateral dimension was equal to 37 mm. Moreover, the size of the acquired BUS images along the axial dimension was within the range of 35 to 55 mm with mean \pm standard deviation of 42.3 ± 6.0 mm. The acquired BUS images had an isotropic resolution with values within the range of 0.062 to 0.097 mm and mean \pm standard deviation of 0.075 ± 0.011 . All acquired BUS images were resampled to obtain a uniform, isotropic resolution of 0.1 mm. In fact, the segmentation method proposed in the current study as well as the existing segmentation methods employed to perform the performance comparisons were applied to the resampled BUS images. The mean \pm standard deviation diameter of the tumors was equal to 14.5 ± 6.3 mm. The true standard segmentation of the tumor in a given BUS image was obtained by asking an experienced radiologist (fourth author) with more than 15 years of clinical experience to manually outline the tumor. In particular, for each BUS image, the radiologist outlined the tumor for three times and the true standard segmentation of the tumor is taken as the average of the three manual tumor outlines. Approval to the study protocol was obtained from the Institution Review Board committee at

the Jordan University Hospital, Amman, Jordan. The patients signed written informed consent to the protocol.

2.2. BUS image decomposition into superpixels using the extended SLIC algorithm

The conventional SLIC algorithm ([Achanta et al., 2012](#)) performs iterative clustering to decompose the image into K superpixels, where the value of K is specified by the user. For grayscale images, such as BUS images, the clustering of the pixels is governed by the 3D space defined by the gray-level values and 2D spatial coordinates of the pixels. In particular, the distance, $D_{i,j}$, between two pixels, i and j , can be expressed as [Achanta et al. \(2012\)](#):

$$\begin{aligned} D_{i,j} &= \sqrt{d_{i,j}^{gl^2} + \left(\frac{m}{S} d_{i,j}^s\right)^2}, \\ d_{i,j}^{gl} &= \sqrt{(gl_i - gl_j)^2}, \\ d_{i,j}^s &= \sqrt{(x_i - x_j)^2 + (y_i - y_j)^2}, \end{aligned} \quad (1)$$

where (x_i, y_i) and (x_j, y_j) are the (x, y) coordinates of pixels i and j , respectively, and gl_i and gl_j are the gray-level values of both pixels. The values of $d_{i,j}^{gl}$ and $d_{i,j}^s$ represent the differences in gray level and spatial location, respectively, between pixels i and j . For large superpixels, the value of $D_{i,j}$ can be dominated by its spatial component, $d_{i,j}^s$. To avoid such domination, $d_{i,j}^s$ in [Eq. \(1\)](#) is multiplied by the scaling factor $\frac{m}{S}$, where m is a parameter to control the compactness of the superpixels and S is a parameter that controls the initial spacings between the centers of the superpixels. The value of the latter parameter is computed as $S = \sqrt{N/K}$, where N is the number of pixels in the image and K is the number of superpixels. In [Achanta et al. \(2012\)](#), m was suggested to be between 1 and 40. To enable effective decomposition of the BUS images, m is tuned in the current study by varying its value between 1 and 40, with an increment of 1. For each examined value of m , the conventional SLIC algorithm is used to decompose a set of sixty BUS images into 50 superpixels. This set of images is obtained by randomly selecting thirty benign BUS images and thirty malignant BUS images from the image database described in [Section 2.1](#). For each decomposed image, the boundary recall ratio of the generated superpixels is computed. The boundary recall ratio is defined as the fraction of true, i.e. manual, tumor boundary that falls within a maximum distance of 2 pixels from the boundaries of the generated superpixels ([Achanta et al., 2012](#)). The analysis indicated that the value of m that maximizes the boundary recall ratio of the generated superpixels is equal to 20. Hence, this value of m is employed in the current study.

The inter-pixel distance, $D_{i,j}$, that is described in [Eq. \(1\)](#) does not consider the image contour cue during the decomposition of the BUS images. Such a limitation leads to the generation of superpixels with reduced boundary recall ratio. For example, consider [Fig. 1\(a\)](#) and [\(b\)](#) that show a BUS image of a malignant tumor and the corresponding manual tumor outline, respectively. The decomposition of the image into 50 superpixels using the conventional SLIC algorithm, which employs the inter-pixel distance in [Eq. \(1\)](#), is shown in [Fig. 1\(c\)](#). The generated superpixels do not adhere well to the tumor boundary, which might restrict the capability of using these superpixels to achieve accurate tumor segmentation.

To overcome this limitation, we have extended the SLIC algorithm to incorporate image contour cue. In particular, the BUS image is analyzed to compute an edge map that quantifies the contours in the image. The computation of the edge map is carried out by preprocessing the BUS image using the speckle reducing anisotropic diffusion (SRAD) algorithm ([Yu & Acton, 2002](#)) to suppress ultrasound speckle and preserve the edges. In fact, the SRAD

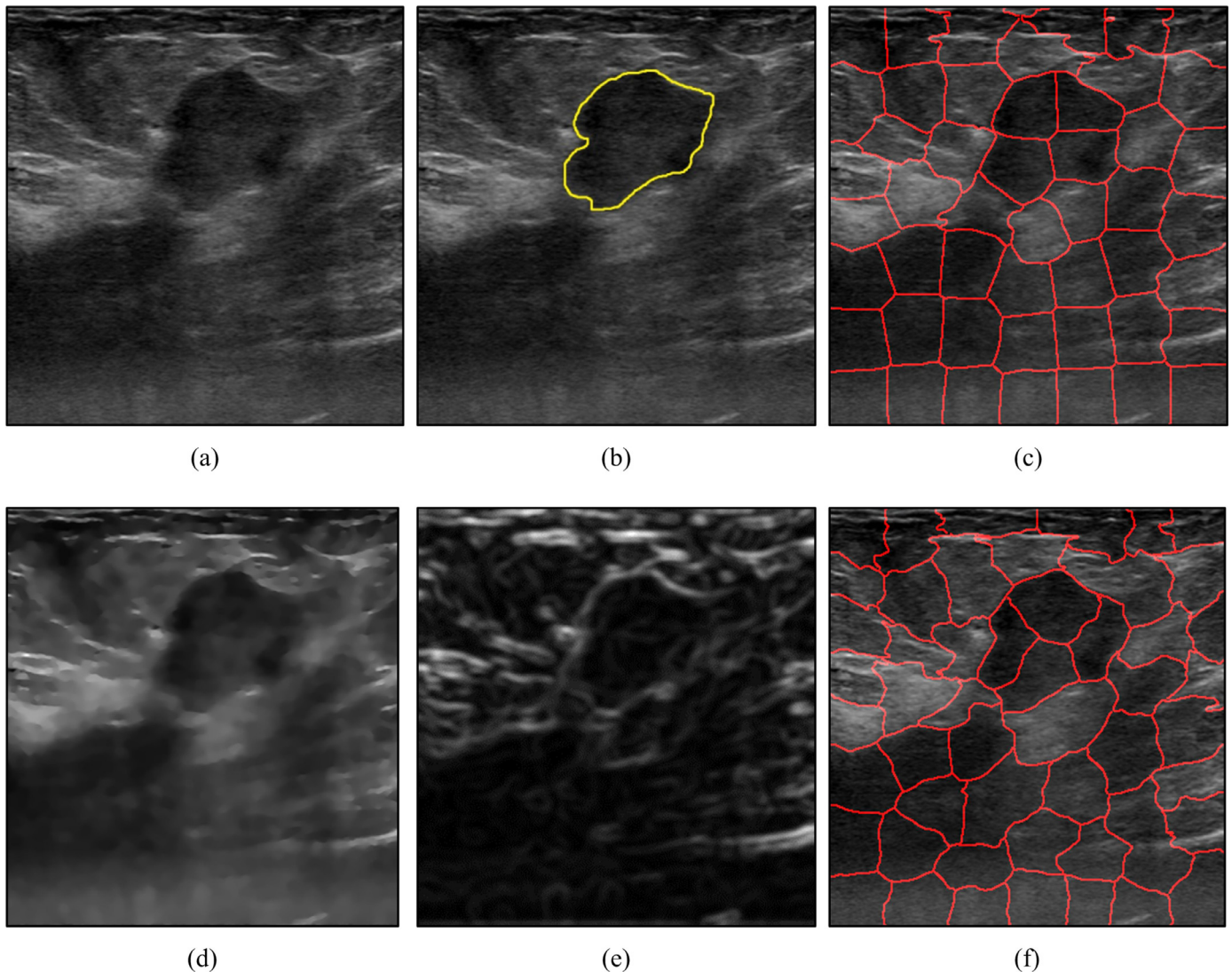


Fig. 1. (a) A BUS image of a malignant tumor, (b) the manual tumor outline, (c) the superpixels generated using the conventional SLIC algorithm, (d) the preprocessed BUS image, (e) the edge map p_{con} , and (f) the superpixels generated by the extended SLIC algorithm.

algorithm is an iterative filtering algorithm that has two parameters, namely the number of iterations and the smoothing time step, where the former controls the degree of smoothing and the latter controls the speed of smoothing. The tuning of the parameters of the SRAD algorithm will be described shortly. The preprocessed BUS image is analyzed using the intervening contour framework, which is described in Leung and Malik (1998), Malik, Belongie, Leung, and Shi (2001), to generate an edge map called p_{con} . The intervening contour framework has two parameters, namely the number of orientations and the number of scales. In this study, the intervening contour framework is configured as described in Malik et al. (2001) by setting the number of orientations to six and the number of scales to three. This parameters configuration of the intervening contour framework enables the edge map, p_{con} , to quantify the edges at six orientations that are uniformly distributed between 0° and 180° and recognize the edges at multiple, complementary scales. The pixels in the edge map, p_{con} , have values that are between 0 and 1. In fact, a value of p_{con} at pixel i , denoted by $p_{con}(i)$, that is close to 1 indicates a strong edge at pixel i . On the contrary, a weak edge is detected at pixel i if the value of $p_{con}(i)$ is around 0. The tuning of the SRAD parameters is carried out with the goal of maximizing the capability of detecting

the edges of the tumor boundary. In particular, the number of iterations parameter is varied between 10 and 100 with an increment of 10 and the smoothing time step parameter is varied between 0.1 and 1.0 with an increment of 0.1. For each examined combination of the two SRAD parameters, the SRAD algorithm and the intervening contour framework were applied to compute the edge map, p_{con} , for each image in the set of sixty randomly-selected BUS images described above. Moreover, for each image in the set of sixty randomly-selected BUS images, a metric, called the edge ratio, is computed by dividing the sum of p_{con} values of the pixels that are located within five pixels from the manual tumor outline over the sum of p_{con} values of the pixels that are separated from the manual tumor outline by six to twenty pixels. The tuned parameters of the SRAD algorithm were obtained by finding the parameters combination of SRAD that maximizes the sum of the edge ratios of all images in the set of sixty randomly-selected BUS images. Based on this tuning procedure, the SRAD configuration that improves the capability of detecting the edges of the tumor boundary is obtained by setting the number of iterations parameter to 50 and the smoothing time step parameter to 0.5. Hence, these values of the SRAD parameters are employed in the rest of the study. Fig. 1(d) and (e) present the preprocessed image and the edge map, respec-

tively, that are computed for the BUS image in Fig. 1(a). After computing the edge map p_{con} , a new distance between pixels i and j , denoted by $d_{i,j}^e$, can be defined based on the image contour cue as follows:

$$d_{i,j}^e = \max_{p \in L_{i,j}} p_{con}(p), \quad (2)$$

where $L_{i,j}$ represents the set of pixels located along the line extending between pixels i and j . The value of $d_{i,j}^e$ is proportional to the maximum p_{con} computed across $L_{i,j}$. Hence, if pixels i and j are separated by a strong edge, then $d_{i,j}^e$ is close to 1. Also, if the two pixels are separated by weak edges, then the value of $d_{i,j}^e$ is close to 0.

The extended SLIC algorithm clusters the pixels of the BUS image based on a four-dimensional space that includes the gray-level values, the 2D spatial positions of the pixels, and the image contour cue that is quantified using $d_{i,j}^e$. Hence, the computation of the distance, $D_{i,j}$, between pixels i and j can be redefined as follows:

$$D_{i,j} = \sqrt{d_{i,j}^{gl^2} + \left(\frac{m}{S} d_{i,j}^s\right)^2 + (\alpha d_{i,j}^e)^2}, \quad (3)$$

where α is a coefficient to control the weight of $d_{i,j}^e$. The tuning of the coefficient α is achieved by varying its value between 1 and 100, with an increment of 1, and employing the extended SLIC algorithm to decompose the set of sixty randomly-selected BUS images, which is described above, into 50 superpixels. For each examined value of the coefficient α , the mean boundary recall ratio of the generated superpixels is computed. The analysis indicated that the extended SLIC algorithm achieved the highest mean boundary recall ratio by setting the coefficient α to 48. Hence, this value of the coefficient α is employed in the rest of the study. Fig. 1(f) presents the superpixels obtained by employing the extended SLIC algorithm to decompose the BUS image in Fig. 1(a) into 50 superpixels. The superpixels in Fig. 1(f) adhere well to the tumor boundary.

To compare the performance of the conventional SLIC algorithm (Achanta et al., 2012) with the extended SLIC algorithm, both algorithms are used to decompose each image in the set of sixty randomly-selected BUS images into $K = \{25, 50, 75, 100, 150, 200, 250, 300\}$ superpixels. The performance of each algorithm is evaluated by computing the boundary recall ratios of the superpixels generated at every examined value of K . The mean \pm standard deviation values of the boundary recall ratios computed for both algorithms as functions of K are shown in Fig. 2(a). The mean values of the boundary recall ratio obtained by the extended SLIC algorithm are higher than the conventional SLIC algorithm for all examined values of K . For both algorithms, the value of the boundary recall ratio increases by decomposing the BUS image into a larger number of fine superpixels. It is worth noting that similar behavior has been reported in Achanta et al. (2012) for the conventional SLIC algorithm. For the extended SLIC algorithm, the improvement in the boundary recall ratio by increasing the number of superpixels is saturated when the number of superpixels reaches 200. In particular, increasing the number of superpixels to 250 and 300 improves the boundary recall ratio by a maximum of 1% compared to the boundary recall ratio obtained by decomposing the BUS image into 200 superpixels. Hence, the extended SLIC algorithm can be configured to generate superpixels that adhere well to the tumor boundary by setting the number of superpixels to 200.

Despite the fact that decomposing the BUS image into a large number of fine superpixels can lead to high boundary recall ratio, the capability of classifying the generated superpixels as tumor or background tissue might be reduced when small superpixels are employed. Therefore, the relationship between the number of su-

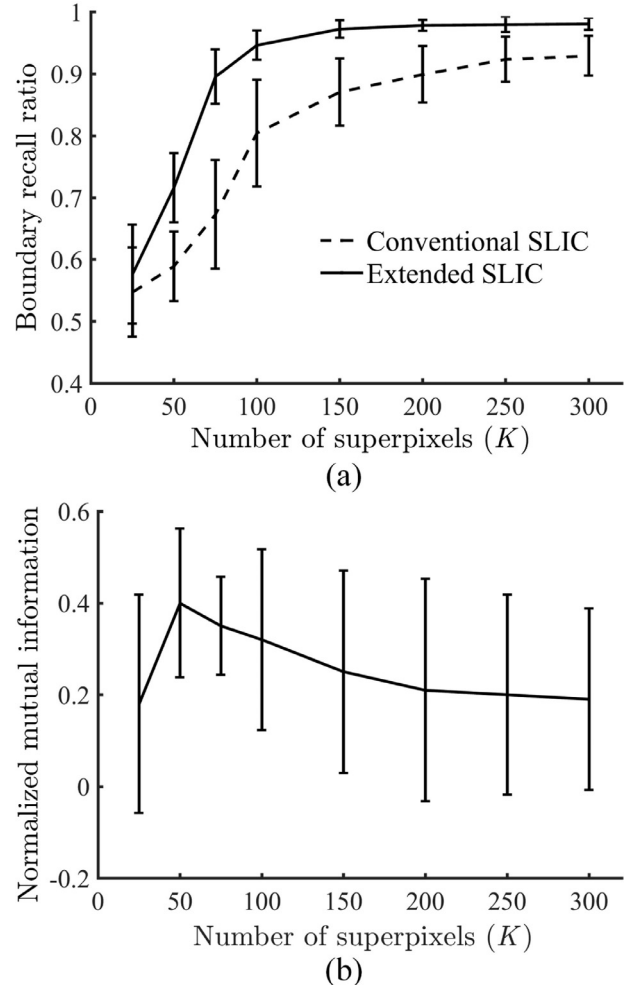


Fig. 2. (a) The mean \pm standard deviation values of the boundary recall ratios obtained by the conventional SLIC algorithm (Achanta et al., 2012) and the extended SLIC algorithm with respect to the number of superpixels, K . (b) The mean \pm standard deviation values of the normalized mutual information between the posterior tumor likelihoods estimated for the superpixels generated by the extended SLIC algorithm and the true labels of the superpixels as a function of number of superpixels, K .

perpixels employed to decompose the BUS image and the capability of correctly classifying the generated superpixels has been investigated. In particular, the extended SLIC algorithm is used to decompose each image in the set of sixty randomly-selected BUS images into $K = \{25, 50, 75, 100, 150, 200, 250, 300\}$ superpixels. For each value of K , the superpixels of each BUS image are analyzed to extract seven texture features that are commonly used for tissue classification. Detailed description of these features is provided in Subsection 2.4.2. The texture features extracted from each superpixel are processed using a well-trained support vector machine (SVM) classifier (Vapnik, 2000) to classify the superpixels as tumor or background tissue. The SVM classifier, which is implemented using the LIBSVM library (Fan, Chen, & Lin, 2005), employed the radial basis function (RBF) kernel. In fact, for each value of K , the SVM classifier is tuned using a grid search approach to find the values of the regularization parameter, C , and the RBF kernel parameter, ρ , that achieve the best possible classification accuracy. As suggested in Hsu, Chang, and Lin (2003), the grid search is performed using $C = \{2^{-5}, 2^{-3}, \dots, 2^{15}\}$ and $\rho = \{2^{-15}, 2^{-13}, \dots, 2^3\}$. Moreover, a ten-fold cross-validation approach is employed, in which the superpixels of 90% of the BUS images are used to train the SVM and the superpixels of the remaining

10% of the images are classified by the trained classifier. This process has been repeated for 10 iterations such that the superpixels of all sixty BUS images are classified by the SVM. The posterior tumor likelihood of each superpixel was estimated from the SVM output using Platt's method (Vapnik, 2000). The ground truth labels of the superpixels are obtained based on the manual outlining of the tumors. For each value of K , the capability of classifying the superpixels has been evaluated by computing the mutual information (Cheng & Greiner, 1999) between the tumor likelihoods estimated for all superpixels of the sixty BUS images and the matching ground-truth labels of the superpixels. The mutual information scores computed for the superpixels are normalized such that their maximum is equal to 1.

Fig. 2(b) presents the mean \pm standard deviation mutual information values of the superpixels as a function of K . The highest mutual information between the posterior tumor likelihoods of the superpixels and their matching ground-truth labels is obtained when each BUS is decomposed into 50 superpixels. The figure also indicates that increasing the value of K to values greater than 50 reduces the mutual information. This finding can be attributed to the fact that the capability of correctly classifying a ROI in the ultrasound image, where each superpixel corresponds to a ROI, is inversely proportional to the size of the ROI (Valckx & Thijssen, 1997). Hence, increasing the number of superpixels, which in turn reduces the sizes of the superpixels, leads to degrading the accuracy of predicting the posterior tumor likelihoods of the superpixels. The figure also indicates that the mutual information obtained by decomposing each BUS image into 25 superpixels is lower than the mutual information achieved by performing the decomposition using 50 superpixels. The reason is that some superpixels obtained by carrying out the decomposition using 25 superpixels might cover different tissue types, including both tumor and background tissue. Hence predicting the dominant tissue type included in such coarse superpixels might be challenging.

Fig. 2(a) and (b) suggest that setting the value of K to 50 generates superpixels with rich texture information that supports effective classification of the superpixels. Moreover, the use of a K value of 200 leads to superpixels that adhere well to the tumor boundary. Therefore, the automatic segmentation method proposed in the current study is carried out in two phases. The first phase is focused on achieving an initial, fully-automatic outline of the tumor. Hence, during the first phase, the BUS image is decomposed into 50 superpixels to enable effective differentiation between the superpixels that belong to the tumor and the superpixels of the background tissue. The second phase is focused on improving the segmentation accuracy. Hence, in this phase, the BUS image is decomposed into 200 fine superpixels to achieve superpixels with high boundary recall ratio.

2.3. Overview of the proposed segmentation method

An overview of the proposed segmentation method is provided in Fig. 3. The method is composed of two phases. In the first phase, the BUS image is analyzed to obtain an initial outline of the tumor. In particular, the BUS image is preprocessed to reduce speckle and the preprocessed image is analyzed to compute the edge map. Moreover, the extended SLIC algorithm is employed to decompose the BUS image into 50 coarse superpixels to enable effective classification of the superpixels as tumor or background tissue. Due to the similar intensity between the tumor and the hypoechoic areas in the BUS image, identifying the tumor outline by directly classifying the individual superpixels is often challenging. To overcome this challenge, the superpixels of the BUS image are processed to estimate their likelihoods of belonging to the tumor, i.e. their posterior tumor likelihoods. An initial tumor outline is obtained using a customized graph cuts algorithm that groups the superpixels

based on their posterior tumor likelihoods and the edge map of the BUS image.

The second phase of the proposed method is focused on refining the accuracy of the initial tumor outline. To achieve this goal, the initial outline of the tumor is employed to compute a weighting function and this weighting function is used to enhance the edge map. The extended SLIC algorithm is used to decompose the BUS image into 200 fine superpixels to achieve high boundary recall ratio as described in the previous subsection. Moreover, the superpixels are analyzed to estimate their posterior tumor likelihoods. Similar to the first phase, the superpixels are processed using a custom-made graph cuts algorithm, which integrates the tumor likelihoods of the superpixels and the enhanced edge map, to obtain accurate tumor outline. Finally, an edge-based active contour model is used to smooth the outline.

2.4. Phase I of the proposed segmentation method: Initial tumor segmentation

2.4.1. Preprocessing the BUS image, computing the edge map, and decomposing the BUS image into coarse superpixels

As described in Subsection 2.2, the BUS image is preprocessed using the SRAD algorithm to reduce ultrasound speckle. Moreover, the preprocessed image is analyzed using the intervening contour framework to compute the edge map, p_{con} . The BUS image and the edge map, p_{con} , are analyzed using the extended SLIC algorithm to decompose the BUS image into 50 superpixels. The generated superpixels are denoted by the set $S = \{s_1, s_2, s_3, \dots, s_K\}$. For example, Fig. 3(a), (b), (c), and (d) show a BUS image of a malignant tumor, the preprocessed BUS image, the edge map computed for the preprocessed BUS image, and the decomposition of the BUS image into 50 superpixels, respectively.

2.4.2. Estimating the posterior tumor likelihoods of the superpixels

The estimation of the posterior tumor likelihood of a given superpixel, s_i , is achieved by extracting a set of texture features from the superpixel and analyzing these features using a well-trained classifier. In fact, texture analysis enables effective identification of abnormalities in the BUS image (Daoud et al., 2016a; Gomez-Flores & Ruiz-Ortega, 2016). The texture features employed in this study include the block difference of inverse probabilities (BDIP) feature (Huang, Wang, & Chen, 2006) as well as six gray-level co-occurrence matrix (GLCM) features (Haralick, Shanmugam, & Dinstein, 1973). The BDIP feature, which quantifies the variations of intensity within a block, has been previously employed for characterizing BUS images (Flores, Pereira, & Infantosi, 2015). The computation of the BDIP feature is performed using a block size of 2 pixels \times 2 pixels, as suggested in Flores et al. (2015), Chen, Huang, and Lin (2011). The GLCM quantifies the frequency of co-occurrence of a given pixel intensity value pair as a function of the distance, d , and the orientation angle, θ . Similar to Moon et al. (2013), the computation of the GLCM is carried out using a distance, d , of 1 pixel and four different orientation angles ($\theta = 0^\circ, 45^\circ, 90^\circ, 135^\circ$). Moreover, the number of quantization levels is set to 32. To enable rotation invariant analysis, the four GLCM matrices computed at each orientation angle are averaged into a single matrix, as suggested in Moon et al. (2013). The average GLCM is analyzed to extract six texture features that are commonly used for BUS image analysis (Flores et al., 2015; Gomez, Pereira, & Infantosi, 2012; Moon et al., 2013). These features are the autocorrelation (Soh & Tsatsoulis, 1999), correlation (Soh & Tsatsoulis, 1999), entropy (Soh & Tsatsoulis, 1999), energy (Soh & Tsatsoulis, 1999), sum average (Haralick et al., 1973), and homogeneity (Soh & Tsatsoulis, 1999).

The texture features computed for each superpixel, s_i , are analyzed using a well-trained SVM classifier (Vapnik, 2000) to classify the superpixel as tumor or background tissue. In fact, the SVM

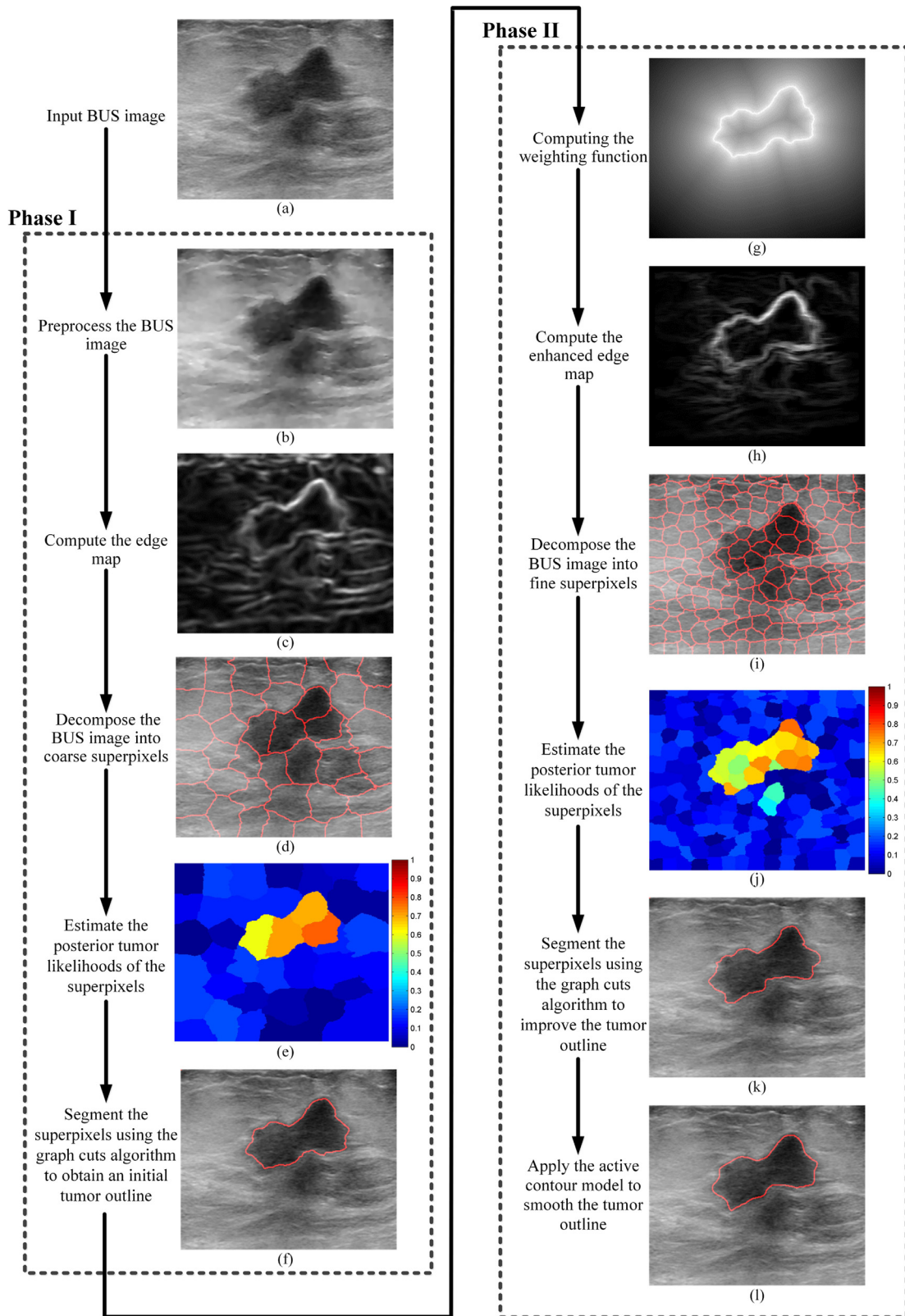


Fig. 3. An overview of the proposed two-phase BUS image segmentation method. (a) A BUS image of a malignant tumor. (b–f) Phase I of the proposed method: (b) the preprocessed BUS image, (c) the edge map, (d) the decomposition of the BUS into coarse superpixels, (e) the tumor likelihoods estimated for the coarse superpixels, and (f) the initial tumor outline obtained by the graph cuts algorithm. (g–l) Phase II of the proposed method: (g) the weighting function that is used to weight the edges in the BUS image, (h) the enhanced edge map, (i) the decomposition of the BUS image into fine superpixels, (j) the posterior tumor likelihoods estimated for the fine superpixels, (k) the refined tumor outline obtained by the customized graph cuts algorithm, and (l) the smoothed tumor outline obtained by the active contour model.

classifier is tuned as described in [Subsection 2.2](#) and the values of the tuned parameters C and ρ are equal to 256 and 2^{-3} , respectively. A ten-fold cross-validation approach is used to classify the superpixels of the BUS images. In particular, the BUS image database is randomly sorted and partitioned into ten groups, such that each group includes 16 images. In each iteration of the cross-validation approach, the superpixels of nine image groups are used to train the SVM and the remaining image group is employed to run the proposed segmentation algorithm, including the application of the trained SVM classifier. This process is repeated for ten times to classify and segment the BUS images of each image group. During training, the ground truth labels of the superpixels in a given BUS image are obtained based on the manually-drawn outline of the tumor. The output of the SVM is analyzed using Platt's approach ([Platt, 1999](#)) to estimate the posterior tumor likelihood, $P_T(s_i)$, of superpixel s_i . The value of $P_T(s_i)$ is within the range of 0 to 1, where 1 represents the highest likelihood value that s_i is tumor and 0 represents the highest likelihood value that s_i is background tissue. [Fig. 3\(e\)](#) shows the posterior tumor likelihoods computed for the superpixels of the decomposed BUS image in [Fig. 3\(d\)](#).

2.4.3. Segmenting the superpixels using the customized graph cuts algorithm

The segmentation of the BUS image can be formulated as a labeling problem based on the graph cuts framework ([Boykov & Jolly, 2001](#)). In particular, consider the set $S = \{s_1, s_2, s_3, \dots, s_K\}$ that represents the superpixels of the BUS image, where K is equal to 50 in the first phase. Let the vector $A = \{a_{s_1}, a_{s_2}, a_{s_3}, \dots, a_{s_K}\}$ be a binary labeling vector whose element a_{s_i} represents the assignment of a label to the superpixel s_i . Each a_{s_i} can be either "T", which denotes the tumor, or "B", which denotes the background tissue. Hence, the vector A describes a segmentation of the BUS image in which each superpixel in the image is labeled as "T" or "B".

The cost function $E(A)$, which represents a soft constraint imposed on the segmentation A , can be formulated to incorporate both region and boundary properties of the superpixels, as expressed below:

$$E(A) = E_{\text{region}}(A) + \gamma \cdot E_{\text{boundary}}(A) \quad (4)$$

where $E_{\text{region}}(A)$ and $E_{\text{boundary}}(A)$ are the region properties term and the boundary properties term, respectively. The coefficient γ is a non-negative weighting parameter that controls the relative importance of $E_{\text{boundary}}(A)$ compared to $E_{\text{region}}(A)$. The region properties term, $E_{\text{region}}(A)$, quantifies how the labels assigned by the segmentation A fit the superpixels of the image. In this study, $E_{\text{region}}(A)$ is computed based on the posterior tumor likelihoods of the superpixels. In particular, $E_{\text{region}}(A)$ can be expressed as:

$$E_{\text{region}}(A) = \sum_{s_i \in S} D_{s_i}(a_{s_i}), \quad (5)$$

where

$$D_{s_i}(a_{s_i} = "T") = -\ln(P_T(s_i)), \quad (6)$$

$$D_{s_i}(a_{s_i} = "B") = -\ln(1 - P_T(s_i)), \quad (7)$$

The quantities $P_T(s_i)$ and $1 - P_T(s_i)$ represent the posterior tumor likelihood and posterior background tissue likelihood, respectively, computed for superpixel s_i . The term $D_{s_i}(a_{s_i})$ quantifies the penalty of assigning the label a_{s_i} to superpixel s_i . If a_{s_i} fits the superpixel s_i , then the value of the negative log of the likelihood should be small, and vice versa.

The boundary properties term, $E_{\text{boundary}}(A)$, aims to ensure piecewise smoothness by encouraging region continuity across the

neighboring superpixels separated by weak tissue boundaries and region discontinuity between the superpixels separated by strong boundaries. Hence, $E_{\text{boundary}}(A)$ can be written as:

$$E_{\text{boundary}}(A) = \sum_{\{s_p, s_q\} \in \aleph} (1 - \delta(a_{s_p}, a_{s_q})) w_{s_p, s_q} \quad (8)$$

In [Eq. \(8\)](#), \aleph is the set of all unordered pairs of neighboring superpixels in S . In fact, any two superpixels that share a common boundary are considered neighboring superpixels. δ is the Kronecker delta function in which $\delta(a_{s_p}, a_{s_q}) = 1$ if $a_{s_p} = a_{s_q}$ and $\delta(a_{s_p}, a_{s_q}) = 0$ otherwise. Hence, the δ function ensures that $E_{\text{boundary}}(A)$ is computed only for neighboring superpixels that are separated by the segmentation. $w_{s_p, s_q} \geq 0$ aims to quantify the edge-based discontinuity between s_p and s_q . In particular, w_{s_p, s_q} should be close to 1 when both superpixels are separated by weak edges and close to 0 when they are separated by strong edges. The computation of w_{s_p, s_q} can be expressed as follows:

$$w_{s_p, s_q} = \exp\left(-\frac{e(s_p, s_q)}{\sigma}\right) \quad (9)$$

where $e(s_p, s_q)$ is the edge score between s_p and s_q and σ is a normalization parameter that weights $e(s_p, s_q)$. The computation of $e(s_p, s_q)$ is performed by identifying the common boundary between s_p and s_q and evaluating the average value of the edge map, p_{con} , along this boundary.

The segmentation of the BUS image can be performed by minimizing the energy function $E(A)$ that is described in [Eq. \(4\)](#). In this study, the minimization of $E(A)$ is carried out by mapping [Eq. \(4\)](#) into a graph $G = (\vee, \xi)$, where \vee and ξ are the sets of nodes and edges, respectively. The set of nodes, \vee , is composed of the image superpixels, S , combined with two additional nodes, $\{s, t\}$. The node s , denoted by the source terminal, represents the tumor and the node t , called the sink terminal, corresponds to background tissue. The set of edges, ξ , is composed of two types of links: terminal links (t -links) and neighborhood links (n -links). Each superpixel is connected to the nodes s and t using two t -links that correspond to the penalty of assigning a particular label to the superpixel. Hence, the weights of the t -links between the superpixel s_i and the nodes s and t are set to $D_{s_i}(a_{s_i} = "T")$ and $D_{s_i}(a_{s_i} = "B")$, respectively. Moreover, each pair of neighboring superpixels, $\{s_p, s_q\} \in \aleph$, is linked using an n -link, which represents the penalty of disconnecting both superpixels. The weight of the n -link between s_p and s_q is equal to $\gamma \cdot w_{s_p, s_q}$. Using this formulation, the t - and n -links in G correspond to the terms $E_{\text{region}}(A)$ and $\gamma \cdot E_{\text{boundary}}(A)$, respectively, in [Eq. \(4\)](#). After constructing the graph G , the tumor outline can be obtained by finding the graph cut with the minimum energy using the min-cut/max-flow algorithm ([Boykov & Jolly, 2001](#)).

The operation of our customized graph cuts algorithm depends on the parameters γ and σ . Therefore, it is important to efficiently tune these two parameters to enable accurate tumor segmentation. In this study, the values of γ and σ are automatically tuned using a grid search approach. In particular, for each BUS image, the value of γ is varied between 0.1 and 1.0 with an increment of 0.1. Moreover, the value of σ is varied between 0.1 and 0.5 with an increment of 0.1. The first phase of our segmentation algorithm is run using these 50 combinations of γ and σ to obtain 50 segmentations of the BUS images, denoted as A_i where $i \in \{1, 2, \dots, 50\}$. Each segmentation is evaluated individually based on the following score metric:

$$\text{score}(A_i) = \text{score}_E(A_i) \times \text{score}_T(A_i), \quad (10)$$

In [Eq. \(10\)](#), $\text{score}_E(A_i)$ and $\text{score}_T(A_i)$ are the edge score and texture score, respectively, of the segmentation, A_i . $\text{score}_E(A_i)$ is the average p_{con} of all pixels located at the tumor outline identified by A_i . Based on this formulation, a value of $\text{score}_E(A_i)$ that is close

to 1 indicates the presence of strong edges at the boundary of A_i , while a value close to 0 indicates weak edges at the boundary of A_i . $score_T(A_i)$ quantifies the texture difference between the boundary superpixels located inside A_i and the boundary superpixels located outside A_i , where a boundary superpixel is the superpixel that has a common boundary with the tumor outline identified by A_i . In this study, $score_T(A_i)$ is computed as follows:

$$score_T(A_i) = \frac{1}{|Q|} \sum_{s_i \in Q} \left(\frac{1}{|P_{s_i}|} \sum_{s_j \in P_{s_i}} HBD(s_i, s_j) \right), \quad (11)$$

where Q is the set of all boundary superpixels located inside A_i , $|\cdot|$ is set size operator, P_{s_i} is the set of boundary superpixels located outside A_i and have a common boundary with s_i , and $HBD(s_i, s_j)$ is the Bhattacharyya distance (Bhattacharyya, 1943) between the histograms of superpixels s_i and s_j . A high value of $score_T(A_i)$ indicates large difference between the textures of the boundary superpixels located inside A_i and the textures of the boundary superpixels located outside A_i . Therefore, the tumor segmentation, A_i , that maximizes $score(A_i)$ in Eq. (10), i.e. maximizes both $score_E(A_i)$ and $score_T(A_i)$, is taken as the tumor outline generated by the first phase of the proposed segmentation method. Fig. 3(f) shows the tumor outline obtained by the first phase of the proposed method for the BUS image presented in Fig. 3(a).

2.5. Phase II of the proposed segmentation method: Tumor segmentation refinement

As mentioned previously, the second phase of the proposed method aims to improve the initial tumor outline obtained by the first phase. This goal has been achieved by employing the initial tumor outline to enhance the edge map of the BUS image, using fine superpixels to achieve high boundary recall ratio, and employing improved estimation of the posterior tumor likelihoods of the superpixels. The fine superpixels are processed using a customized graph cuts algorithm to search the approximate area located around the initial tumor outline and obtain accurate tumor segmentation. Furthermore, an edge-based active contour model is employed to smooth the tumor outline generated by the customized graph cuts algorithm.

2.5.1. Edge map enhancement

The initial tumor outline is used to enhance the edge map by weighting the edges of the BUS image based on their locations with respect to the initial tumor outline. In particular, high weights are assigned to the edges located near the initial tumor outline while small weights are assigned to the edges located away from the initial tumor outline. To perform the weighting, a distance transform, $DT(x, y)$, is computed based on the initial tumor outline. The value of $DT(x, y)$ is equal to the shortest distance between the pixel location, (x, y) , and the initial outline of the tumor. In fact, the computation of $DT(x, y)$ is performed using the low-complexity algorithm described in Maurer, Qi, and Raghavan (2003). After computing $DT(x, y)$, a weighting function, called $W(x, y)$, is defined as follows:

$$W(x, y) = 1 - \frac{DT(x, y)}{\max\{DT(x, y)\}}, \quad (12)$$

where $\max\{DT(x, y)\}$ is the maximum value of $DT(x, y)$ across the entire image. The values of W vary between 1 at the initial tumor outline and 0 at the farthest pixel from the initial tumor outline. The enhancement of the edge map is achieved by multiplying each pixel in the edge map, $p_{con}(x, y)$, by the corresponding pixel in $W(x, y)$. The enhanced edge map is denoted by \hat{p}_{con} . Fig. 3(g) and (h) present the weighting function, $W(x, y)$, and the enhanced edge map, \hat{p}_{con} , respectively, that are computed for the BUS image in Fig. 3(a) based on the initial tumor outline in Fig. 3(f).

2.5.2. Decomposing the BUS image into fine superpixels

The extended SLIC algorithm, which is described in Subsection 2.2, is configured to use the enhanced edge map, \hat{p}_{con} , to decompose the BUS image into 200 superpixels. As described previously, this fine decomposition enables the generation of superpixels with high boundary recall ratio. Moreover, the use of \hat{p}_{con} ensures that the edges located around the initial tumor outline are assigned high weights during the decomposition process. Fig. 3(i) shows the decomposition of the BUS image in Fig. 3(a) into 200 superpixels.

2.5.3. Estimating the posterior tumor likelihoods of the fine superpixels

The posterior tumor likelihood of a fine superpixel s_i , denoted by $\hat{P}_T(s_i)$, is computed based on two components. The first component, denoted by $\hat{P}_T^{fine}(s_i)$, is obtained by analyzing the texture of s_i using the texture-based posterior tumor likelihood procedure described in Subsection 2.4.2. It is worth noting that the SVM classifier employed to carry out the texture-based posterior tumor likelihood procedure is tuned as described in Subsection 2.2 and the values of the tuned parameters C and ρ are equal to 64 and 1, respectively. In fact, the use of a fine superpixel, which corresponds to a small ROI, to perform the texture analysis might limit the ability to quantify the texture patterns inside the superpixel (Valckx & Thijssen, 1997). Such a limitation might affect the capability of accurately estimating the posterior tumor likelihood of the superpixel. To address this limitation, the second component of $\hat{P}_T(s_i)$, denoted by $\hat{P}_T^{coarse}(s_i)$, is based on the posterior tumor likelihoods obtained for the coarse superpixels during the first phase of the proposed method. In particular, let C_{s_i} be the set of coarse superpixels that are generated during the first phase and overlap with the fine superpixel s_i . The value of $\hat{P}_T^{coarse}(s_i)$ is computed as follows:

$$\hat{P}_T^{coarse}(s_i) = \sum_{s_j \in C_{s_i}} P_T(s_j) \frac{Area(s_i \cap s_j)}{Area(s_i)}, \quad (13)$$

where $Area(s_i)$ is the area of the fine superpixel s_i and $Area(s_i \cap s_j)$ is the overlap area between the fine superpixel s_i and the coarse superpixel s_j . In fact, $\hat{P}_T^{coarse}(s_i)$ represents a weighted average of the posterior tumor likelihoods computed for the coarse superpixels that overlap with s_i . After computing $\hat{P}_T^{fine}(s_i)$ and $\hat{P}_T^{coarse}(s_i)$, $\hat{P}_T(s_i)$ is set to be the average of these two components. Fig. 3(j) presents the values of $\hat{P}_T(s_i)$ computed for the fine superpixels in Fig. 3(i).

2.5.4. Segmenting the superpixels using the customized graph cuts algorithm

Since the initial tumor outline, which is obtained by the first phase, is expected to be located within an approximate area that includes the true tumor boundary, the segmentation accuracy can be improved by analyzing the fine superpixels positioned around the initial tumor outline. In fact, this approach enables the second phase to integrate the robust identification of the approximate tumor outline achieved by the first phase with the high boundary recall ratio obtained by the fine superpixels.

To achieve this goal, the 200 fine superpixels are grouped into three sets: marginal superpixels, tumor superpixels, and background superpixels. The set of marginal superpixels is composed of the boundary superpixels, or the superpixels that intersect with the initial tumor outline, and their direct neighboring superpixels. The tumor and background superpixels are the superpixels located inside and outside the initial tumor outline, respectively, and do not belong to the set of marginal superpixels. The tumor and boundary superpixels are assumed to be correctly labeled during the first phase. Moreover, the marginal superpixels are assumed

to synthesize an approximate area that includes the true tumor boundary. Hence, the customized graph cuts algorithm described in Subsection 2.4.3 is used to segment the marginal superpixels to obtain accurate tumor outline. Similar to the first phase, a graph with \vee nodes and ξ edges is constructed. The set \vee includes the 200 fine superpixels, S , as well as the source and sink nodes, $\{s, t\}$. To limit the segmentation to the marginal superpixels, the tumor superpixels and the background superpixels are connected to the source and terminal nodes, respectively, using t -links of infinite strength. Each marginal superpixel, s_i , is connected to the s and t nodes using two t -links with weights of $\hat{D}_{s_i}(a_{s_i} = "T")$ and $\hat{D}_{s_i}(a_{s_i} = "B")$, respectively, where $\hat{D}_{s_i}(a_{s_i} = "T") = -\ln(\hat{P}_T(s_i))$ and $\hat{D}_{s_i}(a_{s_i} = "B") = -\ln(1 - \hat{P}_T(s_i))$. In addition, every marginal superpixel, s_i , is connected to each of its neighboring superpixels, s_j , using an n -link with a weight of $\gamma \cdot \hat{w}_{s_i, s_j}$, where $\hat{w}_{s_i, s_j} = \exp(-\hat{e}(s_i, s_j)/\sigma)$ and $\hat{e}(s_i, s_j)$ is the average edge score between superpixels s_i and s_j computed based on \hat{p}_{con} . Finally, the min-cut/max-flow algorithm is employed to partition the constructed graph and obtain a refined tumor outline. The parameters γ and σ are automatically tuned as described Subsection 2.4.3. Fig. 3(k) presents the refined tumor outline obtained for the BUS image in Fig. 3(a).

2.5.5. Tumor outline smoothing using an edge-based active contour model

The tumor outline generated by the graph cuts algorithm might include some jagged edges. Therefore, the vector field convolution (VFC) active contour model (Li & Acton, 2007) is employed to smooth the tumor outline. In fact, the VFC algorithm is an edge-based active contour model that segments a 2D image based on the edge map of the image. Since the outline obtained by the graph cuts algorithm is expected to be close to the true tumor boundary, the VFC active contour model is constrained to search the local region around the outline generated by the graph cuts algorithm. In particular, the VFC active contour model is configured to employ the tumor outline generated by the graph cuts algorithm as an initial contour and perform the deformation using the enhanced edge map \hat{p}_{con} . Moreover, the active contour elasticity, active contour rigidity, and time step parameters of the VFC active contour model are set, as described in Li and Acton (2007), to 0.5, 0.1, and 0.5, respectively. Furthermore, the VFC active contour model is set to run for a small number of iterations that is equal to 10. In fact, these configurations enabled the VFC active contour model to smooth the jagged edges of the tumor outline obtained by the graph cuts algorithm without over-smoothing the outline or incorrectly driving the outline to edges located away from the true tumor boundary. Fig. 3(l) shows the smoothed tumor outline obtained for the BUS image in Fig. 3(a).

2.6. Performance evaluation

The proposed method was compared with three existing automatic segmentation methods, introduced by Xian et al. (2015), Shan et al. (2012), and Xi et al. (2017), and an existing semi-automatic method, developed by Gao et al. (2012). These four existing methods provide well-studied approaches for segmenting BUS images. The comparisons between the proposed method and the four existing methods were carried out based on the BUS image database described in Subsection 2.1.

In fact, each one of the four existing segmentation methods include parameters and configurations that require careful tuning. As described in the Introduction, the automatic BUS image segmentation method introduced by Xian et al. (2015) includes an adaptive reference point generation procedure, a multipath search to identify the region that includes the tumor, and a graph-based approach to segment the tumor. The automatic method by

Shan et al. (2012) employs a procedure to generate a seed point in the BUS image, a region growing algorithm to identify a ROI that includes the tumor, and a neural network classifier to classify the pixels in the ROI as tumor or background. Furthermore, the automatic method by Xi et al. (2017) decomposes the BUS image into 500 superpixels and applies a level set algorithm combined with a prior knowledge learning model based on a SVM classifier to segment the tumor. The semi-automatic method by Gao et al. (2012) requires the user to manually identify a ROI that includes the tumor. The identified ROI is segmented using texture and boundary analyses combined with the homogeneous patch adaptive neighborhood and the NCut segmentation framework. To enable fair comparisons, we have carefully tuned the parameters of each of the four existing methods, as described in the scientific papers in which these existing methods were introduced, to achieve the best possible tumor segmentation results. For the existing methods that employ a machine learning classifier, including the methods by Shan et al. (2012) and Xi et al. (2017), the classifiers were trained using the produces described in the scientific papers in which these methods were introduced. For the semi-automatic method by Gao et al. (2012), careful consideration has been made to manually select a ROI that is close to the tumor boundary to achieve the highest possible segmentation accuracy.

Our proposed method is compared with the three existing automatic methods, i.e. (Shan et al., 2012; Xian et al., 2015), and Xi et al. (2017), based on the ability of detecting the tumor. Moreover, we have compared our proposed method with the four existing methods, i.e. (Shan et al., 2012; Xi et al., 2017; Xian et al., 2015), and Gao et al. (2012), in terms of the tumor outlining accuracy and execution time.

2.6.1. Tumor detection

The automatic segmentation methods, which include both phases of our proposed method and the three existing automatic methods introduced by Xian et al. (2015), Shan et al. (2012), and Xi et al. (2017), are compared in terms of their ability to detect the tumor. For a given BUS image, the segmentation method is considered to successfully detect the tumor if the tumor outline generated by the method overlaps, partially or completely, with the true tumor region. The numbers of benign and malignant BUS images in which the tumor is successfully detected are reported for each one of the automatic segmentation methods.

2.6.2. Tumor outlining

Both phases of our proposed segmentation method and the four existing segmentation methods, which include the methods by Xian et al. (2015), Shan et al. (2012), Xi et al. (2017), and Gao et al. (2012), are evaluated in terms of their capability to correctly outline the tumor. The comparison is based on both area and boundary error metrics. The area error metrics aim to evaluate the similarity between the region covered by the computer-generated tumor outline, denoted by A_c , that is obtained using one of the segmentation methods and the matching true tumor region, denoted by A_m , that is outlined manually. The area error metrics employed in the current study are the true positive ratio (TPR), the false positive ratio (FPR), the false negative ratio (FNR), and the similarity ratio (SIR). These metrics can be expressed as follows (Liu et al., 2009; Shan et al., 2012):

$$TPR = \frac{\text{Area}(A_m \cap A_c)}{\text{Area}(A_m)} \quad (14)$$

$$FPR = \frac{\text{Area}(A_m \cup A_c - A_m)}{\text{Area}(A_m)} \quad (15)$$

$$FNR = \frac{\text{Area}(A_m \cup A_c - A_c)}{\text{Area}(A_m)} = 1 - TPR \quad (16)$$

$$SIR = \frac{Area(A_m \cap A_c)}{Area(A_m \cup A_c)} \quad (17)$$

A high value of the *TPR* indicates that a large percentage of the true tumor is covered by A_c . Moreover, a low value of the *FNR* indicates that a small percentage of the true tumor is not covered by A_c . A low value of the *FPR* reveals that small areas of the background tissue are incorrectly covered by A_c . The SIR evaluates the overall performance of tumor segmentation. In fact, SIR can take values between 0 and 1, where a high value, i.e. close to 1, indicates good agreement between A_c and A_m , and vice versa. The mean \pm standard deviation values of the four area error metrics are reported for each segmentation method based on both benign and malignant BUS images.

In addition to the area error metrics, two boundary error metrics, namely the mean absolute error (ME) and the Hausdorff error (HE) (Madabhushi & Metaxas, 2003), are used to quantify the difference between the tumor outlines obtained by each of the computer-based methods and the corresponding true tumor outlines. To compute both metrics, let $P = \{p_1, p_2, \dots, p_\alpha\}$ and $Q = \{q_1, q_2, \dots, q_\eta\}$ represent the computer-generated tumor outline and the true tumor outline, respectively, such that each element in P and Q is a point, i.e. boundary pixel, on the corresponding outline. We compute the distance between each point, p_i , in P and all points in Q . The shortest distance, $d(p_i, Q)$, between p_i and Q can be expressed as:

$$\forall p_i \in P, i = 1, \dots, \alpha, \text{ compute} \\ d(p_i, Q) = \min_j \|p_i - q_j\|, j = 1, \dots, \eta \quad (18)$$

where $\|\cdot\|$ is the Euclidean distance between two points. The metrics ME and HE are defined as the mean and maximum values, respectively, of $d(p_i, Q)$ over all i . Hence, the ME and HE metrics evaluate the mean disagreement and the worst disagreement, respectively, between the two outlines. The mean \pm standard deviation values of the ME and HE metrics are reported for each segmentation method using both benign and malignant BUS images.

2.6.3. Execution time

The two phases of our proposed segmentation method and the four existing methods introduced by Xian et al. (2015), Shan et al. (2012), Xi et al. (2017), and Gao et al. (2012) are compared based on their execution times. To perform the comparison, our proposed method and the four existing methods were implemented using MATLAB (MathWorks Inc., Natick, MA, United States) and run on a computer (HP Pavilion HPE h9-1215t Phoenix Desktop, Hewlett-Packard Company, Palo Alto, CA, United States) that has an Intel Core i7-3770K Quad-Core 3.5 GHz processor (Intel Corporation, Santa Clara, CA, United States) and 16 GB of memory. Furthermore, the mean \pm standard deviation execution time required by each method to segment a single BUS image is reported.

3. Experimental results

3.1. Qualitative results

Figs. 4–8 present the tumor outlining results obtained for five representative BUS images that have various characteristics. In particular, Figs. 4 and 5 present two BUS images of malignant tumors, where the former image shows acoustic shadowing underneath the tumor and the latter shows complex tissue background around the tumor. Figs. 6–8 present BUS images of benign tumors, where the first image includes a tumor with non-uniform texture, the second image shows a small tumor with complex background, and the third image includes a tumor in the upper part of the image and

a tumor-like structure in the lower part. In each figure, (a) is the original BUS image along with the manual tumor outline drawn by experienced radiologist (fourth author), (b) and (c) are the outlines generated by the first phase and second phase, respectively, of our proposed segmentation method, and (d), (e), (f), and (g) are the outlines obtained by the methods introduced by Xian et al. (2015), Shan et al. (2012), Xi et al. (2017), and Gao et al. (2012), respectively. As shown in the figures, the first phase of our proposed method enables effective detection and segmentation of the tumor. Moreover, the second phase refines the outline of the first phase to improve the accuracy of tumor segmentation. The tumor outlines obtained by the four previous methods have lower quality than the outlines generated using the two phases of our proposed method. These representative examples demonstrate the improved capability of our proposed method to accurately outline breast tumors that have various sizes, shapes, and tissue backgrounds.

3.2. Tumor detection results

The tumor detection results obtained by the two phases of our proposed method and the automatic segmentation methods introduced by Xian et al. (2015), Shan et al. (2012), and Xi et al. (2017) are provided in Table 1. The tumor outlines generated by the two phases of our proposed method cover, partially or completely, the true tumor regions of all BUS images in the database (86 benign and 74 malignant BUS images). However, the methods introduced by Xian et al. (2015), Shan et al. (2012), and Xi et al. (2017) were able to detect the tumor in 82, 79, and 81 benign BUS images, respectively, and 67, 64, and 65 malignant BUS images, respectively. These results demonstrate the improved capability of our proposed method, particularly the first phase, to effectively detect the tumor and avoid faulty detection of other tumor-like structures in the BUS image. It is worth noting that the number of BUS images in which the true tumor region is correctly detected by the proposed method and the three previous automatic segmentation methods is equal to 141 (79 benign and 62 malignant BUS images). Hence, these 141 BUS images are employed to obtain the tumor outlining results and executions time computations described in the following two subsections.

3.3. Tumor outlining results

The tumor outlining results obtained by each phase of our proposed method, the three automatic methods by Xian et al. (2015), Shan et al. (2012), and Xi et al. (2017), and the semi-automatic method by Gao et al. (2012) are presented in Tables 2 and 3 in terms of the area error metrics and boundary error metrics, respectively. Both tables show that the first phase of the proposed method achieved better performance than the four previous methods independently of the tumor type. When the first phase of the proposed method is compared with the four previous methods based on the benign BUS images, the improvements in the mean TPR, FPR, FNR, SIR, HE, and ME values are equal to 8.83%, 11.96%, 55.70%, 7.92%, 44.36%, and 45.95%, respectively, for the method by Xian et al. (2015), 8.59%, 58.20%, 55.04%, 15.14%, 52.10%, and 59.42%, respectively, for the method by Shan et al. (2012), 15.31%, 44.34%, 67.30%, 31.36%, 67.03%, and 61.56%, respectively, for the method by Xi et al. (2017), and 16.93%, 11.76%, 69.18%, 7.51%, 42.49%, and 52.93%, respectively, for the method by Gao et al. (2012). Furthermore, the improvements in the mean TPR, FPR, FNR, SIR, HE, and ME values obtained by the first phase compared to the previous methods based on the malignant BUS images are equal to 7.12%, 39.58%, 34.52%, 13.03%, 32.83%, and 38.86%, respectively, for the method by Xian et al. (2015), 4.48%, 67.52%, 25.40%, 15.35%, 39.88%, and 51.81%, respectively, for the method by Shan et al. (2012), 17.82%, 57.90%, 54.55%, 34.84%,

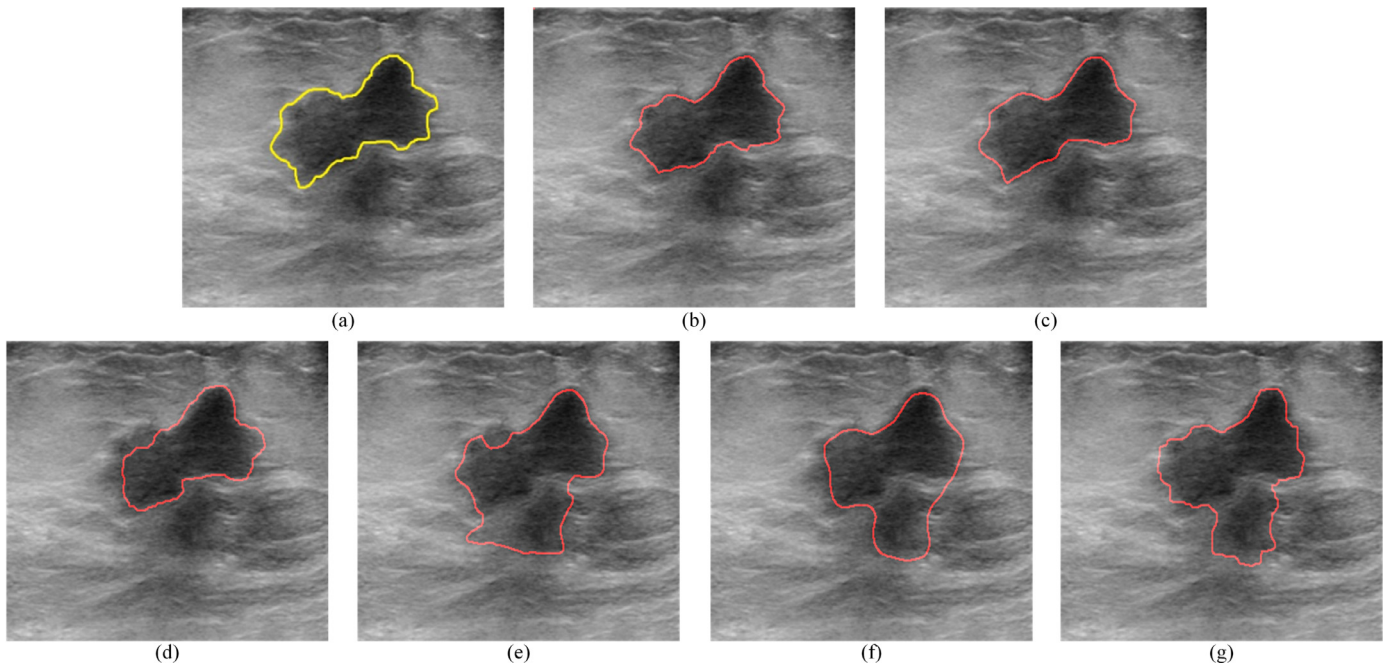


Fig. 4. The segmentation of a BUS image that includes malignant tumor: (a) The original image with manual tumor outline drawn by an experienced radiologist, (b)-(c) the tumor outlines generated by (b) the first phase and (c) the second phase of the proposed method, (d)-(g) the tumor outlines generated by the segmentation methods in (d) (Xian et al., 2015), (e) (Shan et al., 2012), (f) (Xi et al., 2017), and (g) (Gao et al., 2012).

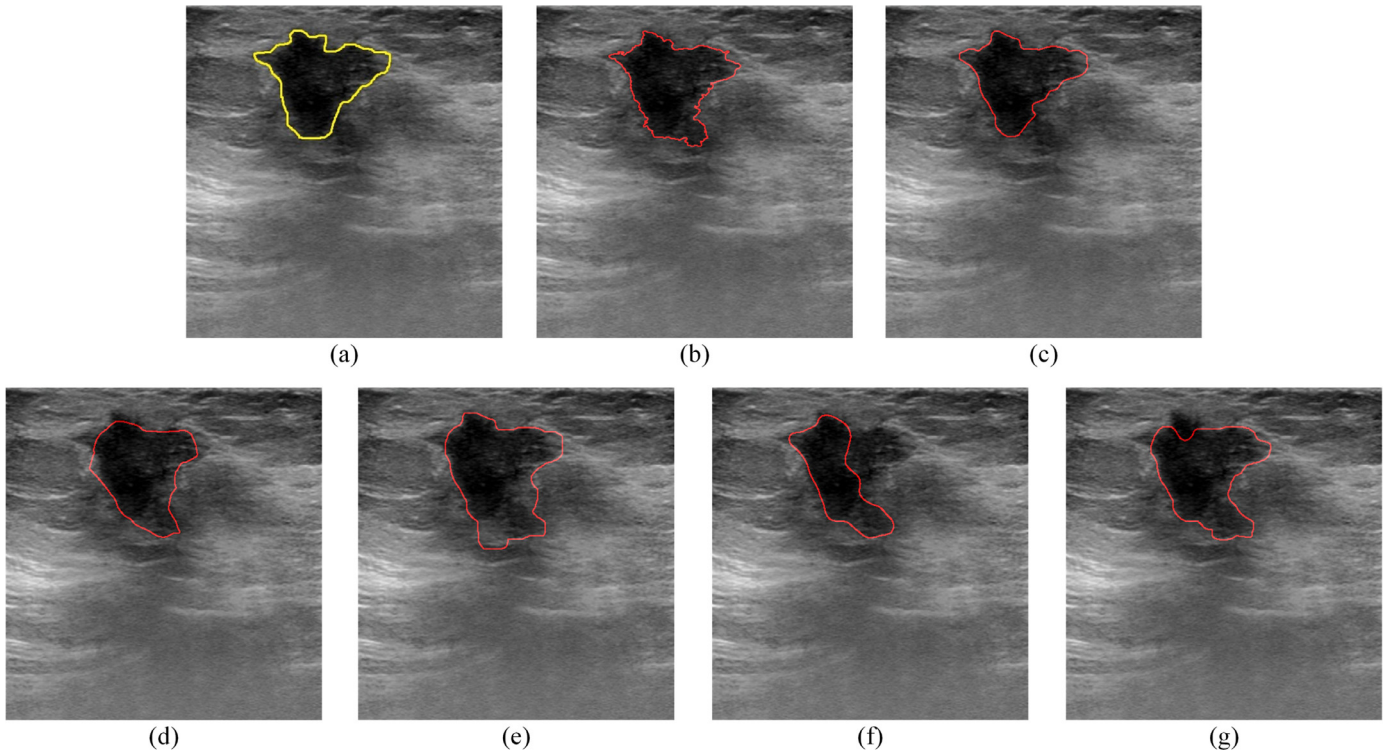


Fig. 5. The segmentation of a BUS image that includes malignant tumor: (a) The original image with manual tumor outline drawn by an experienced radiologist, (b)-(c) the tumor outlines generated by (b) the first phase and (c) the second phase of the proposed method, (d)-(g) the tumor outlines generated by the segmentation methods in (d) (Xian et al., 2015), (e) (Shan et al., 2012), (f) (Xi et al., 2017), and (g) (Gao et al., 2012).

54.87%, and 61.93%, respectively, for the method by [Xi et al. \(2017\)](#), and 12.30%, 29.81%, 46.51%, 7.08%, 30.23%, and 45.37%, respectively, for the method by [Gao et al. \(2012\)](#). [Tables 2](#) and [3](#) also indicate that the second phase of the proposed method improved the tumor outline obtained by the first phase. In particular, the mean TPR, FPR, FNR, SIR, HE, and ME values obtained by the second

phase are better than the first phase by 2.38%, 34.90%, 36.96%, 7.02%, 29.57%, and 21.07%, respectively, for benign tumors and 7.94%, 18.10%, 63.00%, 9.64%, 37.35%, and 22.50% respectively, for malignant tumors.

The results reported in [Tables 2](#) and [3](#) indicate that, for all error metrics except the FPR, the first phase of the proposed method

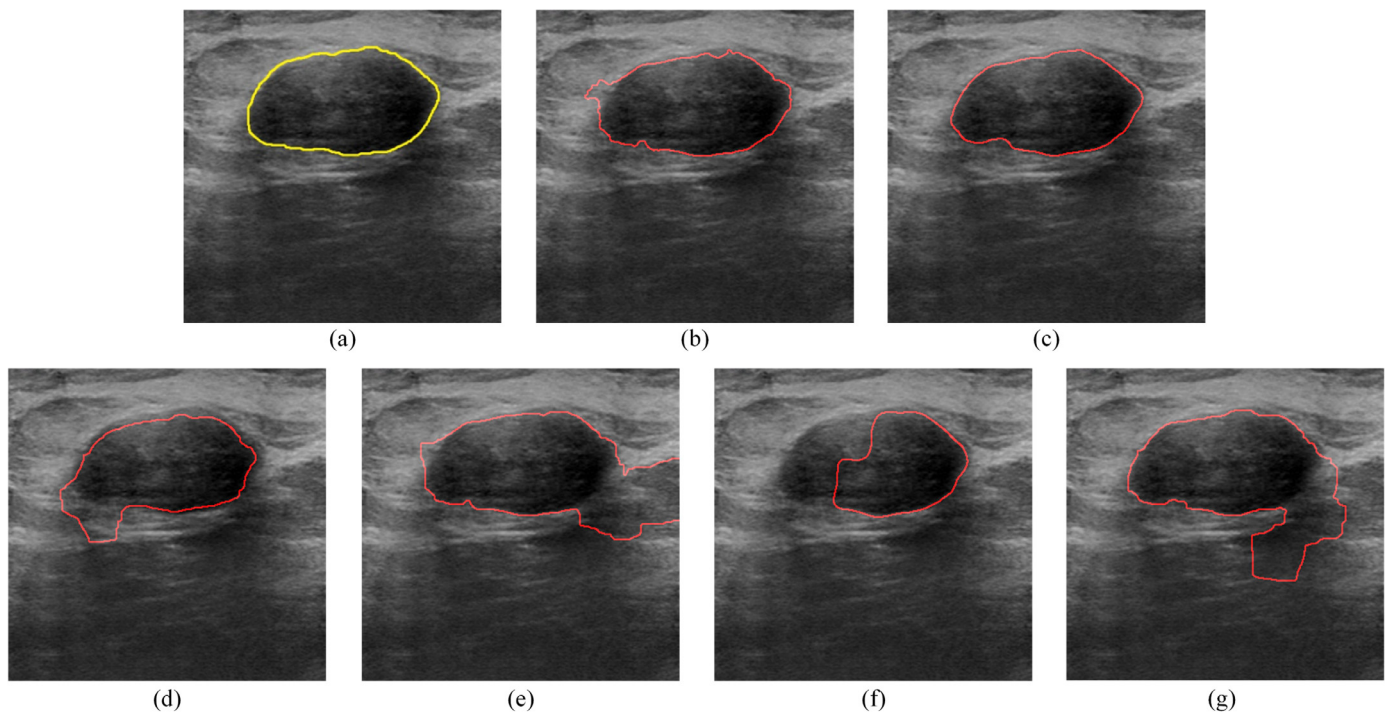


Fig. 6. The segmentation of a BUS image that includes a benign tumor: (a) The original image with manual tumor outline drawn by an experienced radiologist, (b)–(c) the tumor outlines generated by (b) the first phase and (c) the second phase of the proposed method, (d)–(g) the tumor outlines generated by the segmentation methods in (d) (Xian et al., 2015), (e) (Shan et al., 2012), (f) (Xi et al., 2017), and (g) (Gao et al., 2012).

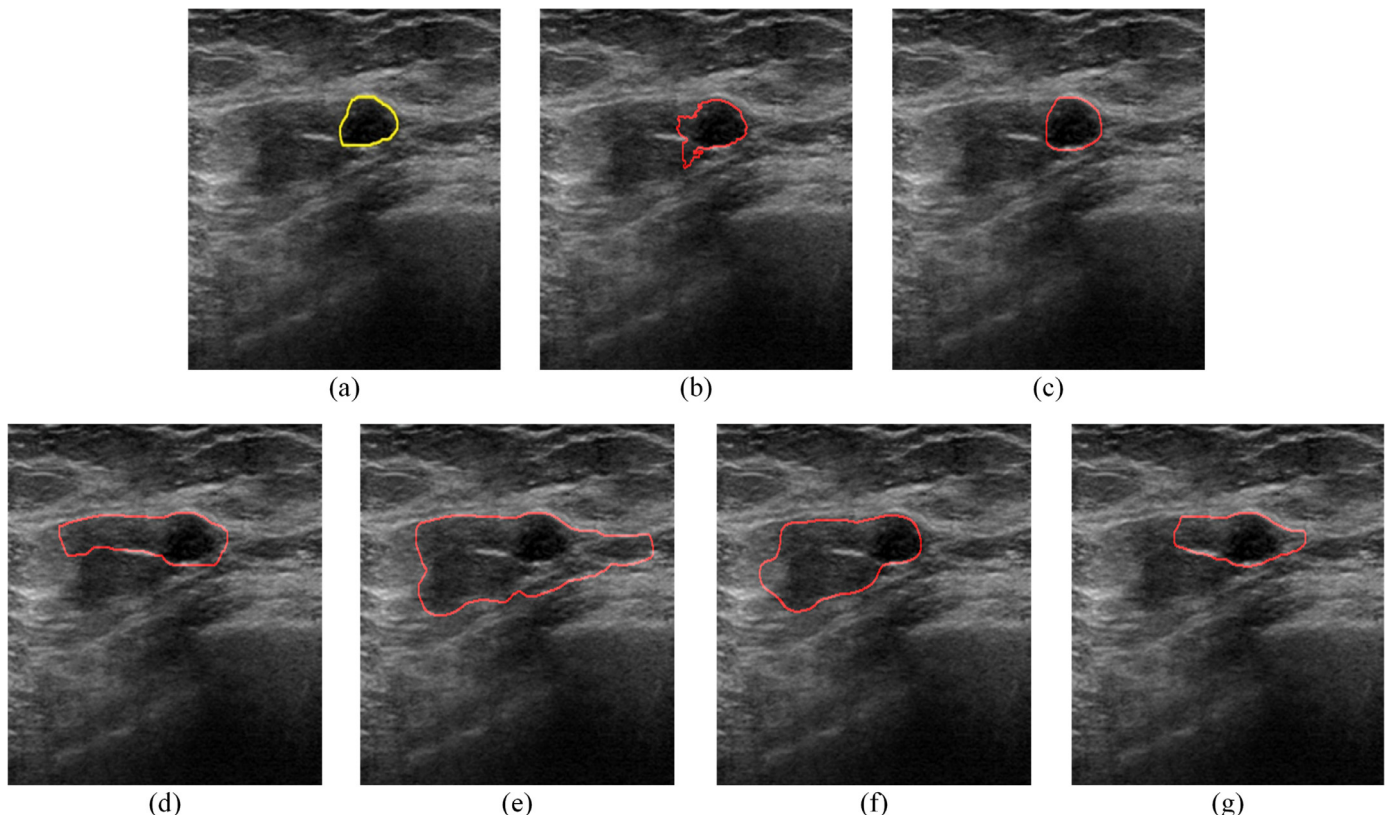


Fig. 7. The segmentation of a BUS image that includes benign tumor: (a) The original image with manual tumor outline drawn by an experienced radiologist, (b)–(c) the tumor outlines generated by (b) the first phase and (c) the second phase of the proposed method, (d)–(g) the tumor outlines generated by the segmentation methods in (d) (Xian et al., 2015), (e) (Shan et al., 2012), (f) (Xi et al., 2017), and (g) (Gao et al., 2012).

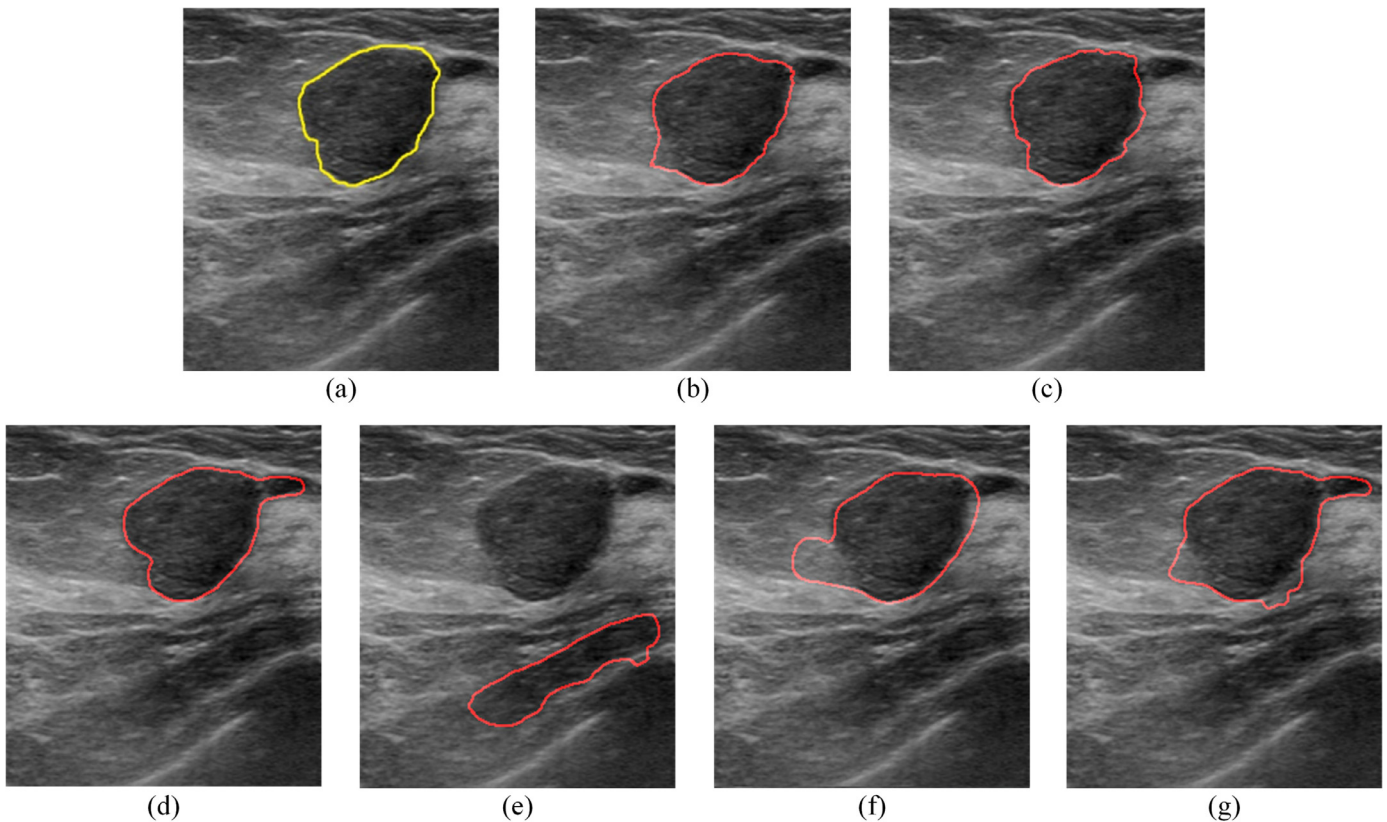


Fig. 8. The segmentation of a BUS image that includes benign tumor: (a) The original image with manual tumor outline drawn by an experienced radiologist, (b)-(c) the tumor outlines generated by (b) the first phase and (c) the second phase of the proposed method, (d)-(g) the tumor outlines generated by the segmentation methods in (d) (Xian et al., 2015), (e) (Shan et al., 2012), (f) (Xi et al., 2017), and (g) (Gao et al., 2012).

Table 1

The numbers of benign and malignant BUS images in which the tumor is correctly detected by the first phase and second phase of the proposed method and the three automatic segmentation methods introduced by Xian et al. (2015), Shan et al. (2012), and Xi et al. (2017).

Number of BUS images	Proposed method first phase	Proposed method second phase	Method in Xian et al. (2015)	Method in Shan et al. (2012)	Method in Xi et al. (2017)
Benign 86	86 (100%)	86 (100%)	82 (95.35%)	79 (91.86%)	81 (94.19%)
Malignant 74	74 (100%)	74 (100%)	67 (90.54%)	64 (86.49%)	65 (87.84%)
Total 160	160 (100%)	160 (100%)	149 (93.13%)	143 (89.38%)	146 (91.25%)

Table 2

The tumor outlining results of the two phases of the proposed method and the four methods introduced by Xian et al. (2015), Shan et al. (2012), Xi et al. (2017), and Gao et al. (2012) in terms of the area error metrics.

	Tumor type	Proposed method first phase	Proposed method second phase	Method in Xian et al. (2015)	Method in Shan et al. (2012)	Method in Xi et al. (2017)	Method in (Gao et al., 2012)
TPR	Benign	93.94 ± 5.32	96.18 ± 2.91	86.32 ± 9.16	86.51 ± 10.07	81.47 ± 17.92	80.34 ± 18.55
	Malignant	88.81 ± 7.74	95.86 ± 1.53	82.91 ± 11.31	85.00 ± 11.87	75.38 ± 21.54	79.08 ± 19.72
	Total	91.68 ± 6.96	96.04 ± 2.40	84.82 ± 10.26	85.85 ± 10.88	78.76 ± 19.78	79.79 ± 19.02
FPR	Benign	12.15 ± 10.73	7.91 ± 6.95	13.80 ± 13.37	29.07 ± 11.14	21.83 ± 20.64	13.77 ± 9.10
	Malignant	9.89 ± 8.74	8.10 ± 5.61	16.37 ± 8.91	30.45 ± 9.64	23.49 ± 22.49	14.09 ± 7.64
	Total	11.16 ± 9.90	7.99 ± 6.37	14.93 ± 11.66	29.68 ± 10.49	22.50 ± 21.37	13.91 ± 8.46
FNR	Benign	6.06 ± 5.32	3.82 ± 2.91	13.68 ± 9.16	13.48 ± 10.07	18.53 ± 17.92	19.66 ± 18.55
	Malignant	11.19 ± 7.74	4.14 ± 1.53	17.09 ± 11.31	15.00 ± 11.87	24.62 ± 21.54	20.92 ± 19.72
	Total	8.32 ± 6.96	3.96 ± 2.40	15.18 ± 10.26	14.15 ± 10.88	21.24 ± 19.78	20.21 ± 19.02
SIR	Benign	85.70 ± 4.82	91.72 ± 2.01	79.41 ± 6.64	74.43 ± 6.13	65.24 ± 17.65	79.71 ± 14.70
	Malignant	83.02 ± 4.73	91.02 ± 2.32	73.45 ± 10.45	71.97 ± 9.33	61.57 ± 15.75	77.53 ± 16.53
	Total	84.52 ± 4.95	91.41 ± 2.17	76.79 ± 9.00	73.35 ± 7.77	63.60 ± 16.87	78.75 ± 15.51

Table 3

The tumor outlining results of the two phases of the proposed method and the four methods introduced by Xian et al. (2015), Shan et al. (2012), Xi et al. (2017), and Gao et al. (2012) in terms of the boundary error metrics.

	Tumor type	Proposed method first phase	Proposed method second phase	Method in Xian et al. (2015)	Method in Shan et al. (2012)	Method in Xi et al. (2017)	Method in Gao et al. (2012)
HE	Benign	14.71 ± 7.18	10.36 ± 5.14	26.44 ± 13.37	30.71 ± 13.88	44.62 ± 33.45	25.58 ± 26.07
	Malignant	21.26 ± 9.84	13.32 ± 4.93	31.65 ± 16.33	35.36 ± 16.25	47.11 ± 23.31	30.47 ± 26.58
	Total	17.59 ± 9.03	11.66 ± 5.24	28.73 ± 14.92	32.75 ± 15.09	45.73 ± 29.29	27.73 ± 26.32
ME	Benign	3.94 ± 1.90	3.11 ± 1.20	7.29 ± 3.75	9.71 ± 4.21	10.25 ± 8.96	8.37 ± 8.32
	Malignant	5.60 ± 2.79	4.34 ± 1.20	9.16 ± 5.84	11.62 ± 5.66	14.71 ± 12.94	10.25 ± 8.57
	Total	4.67 ± 2.47	3.65 ± 1.34	8.11 ± 4.85	10.55 ± 4.97	12.24 ± 11.09	9.20 ± 8.45

Table 4

The mean ± standard deviation execution times of the first and second phases of the proposed method and the four previous methods introduced by Xian et al. (2015), Shan et al. (2012), Xi et al. (2017), and Gao et al. (2012).

	Proposed method first phase	Proposed method second phase	Method in Xian et al. (2015)	Method in Shan et al. (2012)	Method in Xi et al. (2017)	Method in Gao et al. (2012)
Execution time (s)	11.2 ± 0.5 s	23.1 ± 1.2 s	13.2 ± 1.1 s	11.4 ± 2.2 s	13.5 ± 1.8 s	45.5 ± 6.8 s

obtained better segmentation results for benign tumors compared to malignant tumors. The second phase of the proposed method and the four previous segmentation methods achieved better performance for benign tumors than malignant tumors in terms of all error metrics. This finding can be attributed to the fact that benign tumors have, in general, well-defined margins compared to malignant tumors (Chen, Chiou, Chou, & et al., 2009).

3.4. Execution time results

The execution times of the first and second phases of the proposed method and the four previous segmentation methods are provided in Table 4. The mean execution time of the first phase of the proposed method is lower than the four previous methods. Furthermore, the execution time of the complete proposed method, i.e. the sum of the execution times of both phases, is around 34.3 s, which is higher than the automatic methods by Xian et al. (2015), Shan et al. (2012), and Xi et al. (2017) and lower than the semi-automatic method by Gao et al. (2012). In fact, these results demonstrate the feasibility of employing our proposed segmentation method to accurately outline the tumors in BUS images at interactive rates.

4. Discussion

Unlike most previous BUS image segmentation methods, the proposed method is based on decomposing the BUS image into a set of superpixels and grouping the superpixels into two categories: tumor and background tissue. This superpixel-based approach enables the extraction of texture features from subregions, i.e. superpixels, in the BUS image that have relatively homogeneous texture characteristics. These texture features can be used to estimate of the posterior tumor likelihoods of the superpixels. However, a key requirement to enable effective superpixel-based segmentation is to achieve superpixels with high boundary recall ratios. The conventional SLIC algorithm (Achanta et al., 2012) provides an attractive approach to generate superpixels based on the gray level values and positions of the image pixels, but it does not incorporate image contour cue. To address this limitation, we have extended the SLIC algorithm to include an edge map that quantifies the edges in the BUS image. Our extended SLIC algorithm has successfully generated superpixels with boundary recall ratios that are higher than the conventional SLIC algorithm, as demonstrated in Figs. 1 and 2(a).

The first phase of our proposed segmentation method employs coarse superpixels, which support effective texture-based tissue

characterization as indicated in Fig. 2(b), to detect the tumor and obtain an initial tumor outline. In fact, the graph cuts algorithm employed by the first phase combines the edge-based relationships between neighboring superpixels and the region-based information obtained by estimating the posterior tumor likelihoods of the individual superpixels using a SVM classifier. The relative importance between the edge- and region-based information is controlled by the weighting parameter γ , as shown in Eq. (4). Hence, a crucial requirement to achieve accurate BUS image segmentation is to effectively tune γ . To address this requirement, we have tuned the parameter γ using an automatic grid search approach that aims to maximize the edge- and texture-based separations between the superpixels inside the tumor and the superpixels outside the tumor. Our combined edge- and region-based approach has enabled the first phase to correctly detect the tumor in all 160 BUS images examined in this study, as shown in Table 1. Furthermore, Tables 2 and 3 indicate that the tumor segmentation performance obtained by the first phase of our proposed method is higher than the previous methods introduced by Xian et al. (2015), Shan et al. (2012), Xi et al. (2017), and Gao et al. (2012) in terms of the area and boundary error metrics, respectively.

The second phase of the proposed method aims to refine the tumor outline obtained by the first phase. To achieve this goal, the edge map is enhanced based on the initial tumor outline and the BUS image is decomposed into fine superpixels to achieve high boundary recall ratios. Similar to the first phase, the graph cuts algorithm is used to segment the superpixels based on the edge- and region-based information. However, the graph cuts algorithm is configured to limit the segmentation to the local region around the initial tumor outline. The edge-based VFC active contour model is finally used to smooth the tumor outline. Tables 2 and 3 indicate that these enhancements have enabled the second phase of the proposed method to improve the initial tumor outline obtained by the first phase in terms of the area and boundary error metrics.

Compared with previous BUS image segmentation methods that employ superpixels, our proposed method provides an important advancement to enable effective tumor segmentation. For example, the preliminary superpixel-based segmentation method (Daoud et al., 2016a) that was proposed by our group used a simplified region growing procedure to segment the superpixels. In fact, our previous method assumes that the seed superpixel that is used to initiate the region growing procedure is located at a central region of the BUS image. Such assumption prevents the application of this method to many BUS images that we have analyzed in the current study. Another example is the superpixel-based segmentation method by Xi et al. (2017) that decomposes the BUS im-

age into 500 superpixels and analyzes these fine superpixels using prior knowledge and level set segmentation. As shown in Tables 1, 2, and 3, the segmentation results obtained by the first phase and second phase of our proposed method outperform the results obtained by the method introduced by [Xi et al. \(2017\)](#) in terms of the capability of detecting the tumor, the area error metrics, and the boundary error metrics.

The execution time of the first phase of our proposed segmentation method is around 11 s, which is lower than the execution times of the methods introduced by [Xian et al. \(2015\)](#), [Shan et al. \(2012\)](#), [Xi et al. \(2017\)](#), and [Gao et al. \(2012\)](#). The reduced execution time of the first phase is mainly attributed to the use of coarse superpixels, instead of individual pixels, to outline the tumor. However, the execution time of the second phase of our proposed segmentation method is around two times higher than the execution time of the first phase. This can be attributed to fact that the second phase is composed of a graph cuts algorithm that is applied to fine superpixels and an edge-based active contour model that is used to smooth the tumor outline. The execution time of the complete proposed method, i.e. both phases, is around 34.3 s, which is higher than the execution times of the methods introduced by [Xian et al. \(2015\)](#), [Shan et al. \(2012\)](#), and [Xi et al. \(2017\)](#) and lower than the execution time of the method introduced by [Gao et al. \(2012\)](#). The two phase structure of our proposed method allows adaptable configuring of the tumor segmentation process based on the required tumor outline accuracy and the preferred execution time. In particular, the method can be configured to only employ the first phase to obtain accurate tumor outline within short execution time. The accuracy and smoothness of the tumor outline can be improved by applying the second phase, but such configuration requires higher execution time. In the future, we are planning to reduce the execution times of both phases of the proposed method by using parallel computing and graphics processing unit (GPU) technology.

In general, the execution times reported in [Table 4](#) for the existing BUS image segmentation methods are close to or smaller than the execution times reported for these methods in the scientific papers in which they were published. For example, the mean execution times of the methods by [Shan et al. \(2012\)](#) and [Xi et al. \(2017\)](#) as reported in [Table 4](#) are equal to 11.4 s and 13.5 s, respectively, which are close to the execution times of 9.5 s and 8.3 s that are reported for these two methods in [Shan et al. \(2012\)](#) and [Xi et al. \(2017\)](#), respectively. Furthermore, the execution time reported in [Table 4](#) for the method by [Gao et al. \(2012\)](#) is equal to 45.5 s, which is around four times smaller than the execution time of 191.8 s that is reported for the same method in [Gao et al. \(2012\)](#). In fact, the large difference between the execution time reported in the current study for the method by [Gao et al. \(2012\)](#) and the execution time of the same method that is reported in [Gao et al. \(2012\)](#) can be attributed to the fact that the computer used in the current study, which has an Intel Core i7-3770K Quad-Core at 3.5 GHz processor and 16 GB of memory, has higher specifications than the computer employed in [Gao et al. \(2012\)](#), which has an Intel Core 2 7200 at 2 GHz processor and 0.99 GB of memory. It is worth noting that the study in [Xian et al. \(2015\)](#) did not report the total execution time of the BUS image segmentation method introduced in that study.

In the current study, the performance evaluations of our proposed method and the previous BUS image segmentation methods were performed by comparing the tumor outlines generated by these methods with the matching true standard tumor segmentations obtained based on manual outlining of the tumors. In fact, the procedure of obtaining the true standard tumor segmentations based on manual tumor outlines might be affected by both intra-observer variability and inter-observer variability. In the current study, the intra-observer variability of the true

standard tumor segmentations was reduced by asking an experienced radiologist (fourth author) with more than 15 years of clinical experience to outline the tumor in each BUS image for three times and taking the average of the three manual tumor outlines as the true standard tumor segmentation. However, our procedure of obtaining the true standard tumor segmentations did not address the potential inter-observer variability limitation due to the absence of additional experienced radiologists who are willing to outline the tumors in the BUS images. In fact, the procedure of obtaining the true standard tumor segmentations based on manual tumor outlines drawn by a single radiologist has been employed by the majority of studies conducted in the field of BUS image segmentation, such as [Gomez-Flores and Ruiz-Ortega \(2016\)](#), [Gao et al. \(2012\)](#), [Gomez et al. \(2010\)](#), [Liu et al. \(2009\)](#), [Lotfollahi et al. \(2017\)](#), [Madabhushi and Metaxas \(2003\)](#), [Rodrigues et al. \(2015\)](#), [Shan et al. \(2012\)](#), [Wang et al. \(2014\)](#), [Xi et al. \(2017\)](#), [Xian et al. \(2015\)](#), [Xie et al. \(2017\)](#). Nevertheless, one of our future directions is to improve the true standard tumor segmentations by asking multiple experienced radiologists to outline the tumor in each BUS image.

The clinical image database employed in the current study is composed of BUS images acquired using a single ultrasound imaging system, i.e. the Acuson S2000 ultrasound imaging system. In fact, the limited availability of benchmark BUS image databases has restricted our ability to evaluate the performance of the proposed segmentation method, as well as the four previous segmentation methods, on BUS images acquired using different ultrasound imaging systems. Our future plans include extending the image database to include BUS images acquired using different ultrasound systems and evaluate the performance of the proposed method and the four previous methods based on this extended database.

To the best of our knowledge, the vast majority of the previous BUS image segmentation methods, such as [Gomez-Flores and Ruiz-Ortega \(2016\)](#), [Xian et al. \(2015\)](#), [Shan et al. \(2012\)](#), [Liu et al. \(2009\)](#), [Gao et al. \(2012\)](#), [Xi et al. \(2017\)](#), assume that each BUS image includes one tumor. Similar to these previous methods, the formulation of our proposed method and the performance evaluations carried out in the current study are focused on segmenting BUS images that include one tumor. In fact, if the BUS image includes multiple tumors, then the regions in the BUS image that include the individual tumors can be extracted and our proposed segmentation method can be applied to these extracted regions. Hence, if the BUS image includes multiple tumors, then our proposed segmentation method can be applied in a semi-automatic manner. In the future, we are planning to improve our proposed method to support the automatic segmentation of multiple tumors in a single BUS image. As part of this future direction, we will expand our BUS image database to include BUS images with multiple tumors.

5. Conclusion

An automatic two-phase method is proposed to enable accurate segmentation of BUS images. In particular, the proposed method is based on decomposing the BUS image into superpixels with high boundary recall ratio using an extended version of the SLIC algorithm. The first phase of the proposed method aims to detect the tumor and obtain an initial tumor outline. To achieve this goal, the BUS image is decomposed into a set of coarse superpixels to improve the capability of classifying the superpixels using texture analysis. An initial outline of the tumor is obtained by labeling the superpixels as tumor or background tissue using a customized graph cuts algorithm that incorporates edge- and region-based information. The edge-based information represents the edges between the neighboring superpixels and the region-based information quantifies the posterior tumor likelihoods of the superpixels

that are computed using a SVM classifier. The second phase of the proposed method is focused on improving the accuracy of the initial tumor outline. To achieve this objective, the edges of the BUS image are enhanced based on the initial tumor outline. Moreover, the BUS image is decomposed into fine superpixels that have high boundary recall ratios. The customized graph cuts algorithm is used to segment the fine superpixels, such that the segmentation is restricted to an approximate area around the initial tumor outline. Finally, an edge-based active contour model is used to smooth the tumor outline. The performance of both phases of the proposed method is evaluated using an image database that includes 86 benign BUS images and 74 malignant BUS images. The results indicated that the first phase of the proposed method detected the tumor in all BUS images and obtained tumor outlines that outperform four well-studied BUS image segmentation methods in terms of area and boundary error metrics. Furthermore, the results indicated that the second phase of the proposed method has successfully improved the quality of the tumor outlines obtained by the first phase. The results reported in this study suggest that the proposed two-phase segmentation method can be used to enable automatic and accurate segmentation of BUS images within reasonable execution times. Such capability is crucial to achieve automatic and effective CAD systems.

CRediT authorship contribution statement

Mohammad I. Daoud: Conceptualization, Methodology, Software, Validation, Formal analysis, Investigation, Resources, Data curation, Writing - original draft, Writing - review & editing, Visualization, Supervision, Project administration, Funding acquisition. **Ayman A. Atallah:** Conceptualization, Methodology, Software, Validation, Formal analysis, Investigation, Writing - review & editing, Visualization. **Falah Awwad:** Resources, Writing - review & editing. **Mahasen Al-Najjar:** Validation, Investigation, Resources, Data curation, Funding acquisition. **Rami Alazrai:** Resources, Writing - original draft, Writing - review & editing.

Acknowledgments

This research is supported by the Scientific Research Support Fund (project number ICT/2/07/2013), Jordan.

References

- Achanta, R., Shaji, A., Smith, K., Lucchi, A., Fua, P., & Susstrunk, S. (2012). SLIC superpixels compared to state-of-the-art superpixel methods. *IEEE Transactions on Pattern Analysis and Machine Intelligence*, 34, 2274–2281.
- Berg, W. A., Bandos, A. I., Mendelson, E. B., Lehrer, D., Jong, R. A., & Pisano, E. D. (2016). Ultrasound as the primary screening test for breast cancer: Analysis from ACRIN 6666. *JNCI: Journal of the National Cancer Institute*, 108, djv367.
- Bhattacharya, A. (1943). On a measure of divergence between two statistical populations defined by their probability distributions. *Bulletin of the Calcutta Mathematical Society*, 35, 99–109.
- Boykov, Y. Y., & Jolly, M. P. (2001). Interactive graph cuts for optimal boundary & region segmentation of objects in N-D images. In *Proceedings of the eighth IEEE international conference on computer vision* (pp. 105–112).
- Calas, M. J. G., Almeida, R. M. V. R., Gutfilen, B., & Pereira, W. C. A. (2010). Intraobserver interpretation of breast ultrasonography following the BI-RADS classification. *European Journal of Radiology*, 74, 525–528.
- Chang, R. F., Wu, W. J., Moon, W. K., & Chen, D. R. (2003). Improvement in breast tumor discrimination by support vector machines and speckle-emphasis texture analysis. *Ultrasound in Medicine & Biology*, 29, 679–686.
- Chen, C.-Y., Chiou, H.-J., Chou, S.-Y., & et al. (2009). Computer-aided diagnosis of soft-tissue tumors using sonographic morphologic and texture features. *Academic Radiology*, 16, 1531–1538.
- Chen, D., Huang, Y., & Lin, S. (2011). Computer-aided diagnosis with textural features for breast lesions in sonograms. *Computerized Medical Imaging and Graphics*, 35, 220–226.
- Cheng, H. D., Shan, J., Ju, W., Guo, Y., & Zhang, L. (2010a). Automated breast cancer detection and classification using ultrasound images: A survey. *Pattern Recognition*, 43, 299–317.
- Cheng, J., & Greiner, R. (1999). Comparing Bayesian network classifiers. In *Proceedings of the fifteenth conference on uncertainty in artificial intelligence* (pp. 101–108).
- Cheng, J. Z., Chou, Y. H., Huang, C. S., Chang, Y. C., Tiu, C. M., Yeh, F. C., et al. (2010b). ACCOMP: Augmented cell competition algorithm for breast lesion demarcation in sonography. *Medical Physics*, 37, 6240–6252.
- Daoud, M. I., Atallah, A. A., Awwad, F., & Al-Najjar, M. (2016a). Accurate and fully automatic segmentation of breast ultrasound images by combining image boundary and region information. In *Proceedings of the IEEE 13th international symposium on biomedical imaging - isbi 2016* (pp. 718–721).
- Daoud, M. I., Baba, M. M., Awwad, F., Al-Najjar, M., & Tarawneh, E. S. (2012). Accurate segmentation of breast tumors in ultrasound images using a custom-made active contour model and signal-to-noise ratio variations. In *Proceedings of the 8th international conference on signal image technology and internet based systems - sitis 2012* (pp. 137–141).
- Daoud, M. I., Bdair, T. M., Al-Najjar, M., & Alazrai, R. (2016b). A fusion-based approach for breast ultrasound image classification using multiple-ROI texture and morphological analyses. *Computational and Mathematical Methods in Medicine*, 2016, Article ID 6740956, 12 pages.
- de Araujo, A. F., Constantinou, C. E., & Tavares, J. M. (2016). Smoothing of ultrasound images using a new selective average filter. *Expert Systems with Applications*, 60, 96–106.
- Fan, R., Chen, P., & Lin, C. (2005). Working set selection using second order information for training support vector machines. *The Journal of Machine Learning Research*, 6, 1889–1918.
- Perlay, J., Soerjomataram, I., Dikshit, R., Eser, S., Mathers, C., Rebello, M., et al. (2015). Cancer incidence and mortality worldwide: Sources, methods and major patterns in GLOBOCAN 2012. *International Journal of Cancer*, 136, E359–E386.
- Flores, W., Pereira, W., & Infantosi, A. (2015). Improving classification performance of breast lesions on ultrasonography. *Pattern Recognition*, 48, 1125–1136.
- Gao, L., Yang, W., Liao, Z., Liu, X., Feng, Q., & Chen, W. (2012). Segmentation of ultrasonic breast tumors based on homogeneous patch. *Medical Physics*, 39, 3299–3318.
- Garra, B. S., Krasner, B. H., Horii, S. C., Ascher, S., Mun, S. K., & Zeman, R. K. (1993). Improving the distinction between benign and malignant breast lesions: The value of sonographic texture analysis. *Ultrasonic Imaging*, 15, 267–285.
- Gomez, W., Leija, L., Alvarenga, A. V., Infantosi, A. F., & Pereira, W. C. (2010). Computerized lesion segmentation of breast ultrasound based on marker-controlled watershed transformation. *Medical Physics*, 37, 82–95.
- Gomez, W., Pereira, W., & Infantosi, A. (2012). Analysis of co-occurrence texture statistics as a function of gray-level quantization for classifying breast ultrasound. *IEEE Transactions on Medical Imaging*, 31, 1889–1899.
- Gomez-Flores, W., & Ruiz-Ortega, B. A. (2016). New fully automated method for segmentation of breast lesions on ultrasound based on texture analysis. *Ultrasound in Medicine & Biology*, 42, 1637–1650.
- Haralick, R., Shanmugam, K., & Dinstein, I. (1973). Textural features for image classification. *IEEE Transactions on Systems, Man, and Cybernetics*, 3, 610–621.
- Helala, M. A., & Qureshi, F. Z. (2014). Accelerating cost volume filtering using salient subvolumes and robust occlusion handling. In *Proceedings of the Asian conference on computer vision* (pp. 316–331).
- Hsu, C., Chang, C., & Lin, C. (2003). A practical guide to support vector classification. *Technical Report*, Taipei, Taiwan: Department of Computer Science, National Taiwan University.
- Huang, Q., Luo, Y., & Zhang, Q. (2017). Breast ultrasound image segmentation: A survey. *International Journal of Computer Assisted Radiology and Surgery*, 12, 493–507.
- Huang, Y.-L., Wang, K.-L., & Chen, D. (2006). Diagnosis of breast tumors with ultrasonic texture analysis using support vector machines. *Neural Computing and Applications*, 15, 164–169.
- Kaul, K., & Daguillh, F. M. (2002). Early detection of breast cancer: Is mammography enough? *Hospital Physician*, 9, 49–54.
- Kelly, K. M., Dean, J., & Lee, W. S. C. S. J. (2010). Breast cancer detection using automated whole breast ultrasound and mammography in radiographically dense breasts. *European Radiology*, 20, 734–742.
- Kirberger, R. M. (1995). Imaging artifacts in diagnostic ultrasound - a review. *Veterinary Radiology & Ultrasound*, 36, 297–306.
- Kolb, T. M., Lichy, J., & Newhouse, J. H. (2002). Comparison of the performance of screening mammography, physical examination, and breast us and evaluation of factors that influence them: An analysis of 27,825 patient evaluations. *Radiology*, 225, 165–175.
- Leconte, I., Feger, C., Galant, C., Berlire, M., Berg, B. V., D'Hoore, W., & Maldague, B. (2003). Mammography and subsequent whole-breast sonography of nonpalpable breast cancers: The importance of radiologic breast density. *American Journal of Roentgenology*, 180, 1675–1679.
- Leung, T., & Malik, J. (1998). Contour continuity in region based image segmentation. In *Proceedings of the euro. conf. computer vision* (pp. 544–559).
- Li, B., & Acton, S. (2007). Active contour external force using vector field convolution for image segmentation. *IEEE Transactions on Image Processing*, 16, 2096–2106.
- Liu, B., Cheng, H. D., Huang, J., Tian, J., Liu, J., & Tang, X. (2009). Automated segmentation of ultrasonic breast lesions using statistical texture classification and active contour based on probability distance. *Ultrasound in Medicine & Biology*, 35, 1309–1324.
- Lotfollahi, M., City, M., Ye, J., & Far, A. (2017). Segmentation of breast ultrasound images based on active contours using neutrosophic theory. *Journal of Medical Ultrasonics*, 1–8.

- Madabhushi, A., & Metaxas, D. N. (2003). Combining low-, high-level and empirical domain knowledge for automated segmentation of ultrasonic breast lesions. *IEEE Transactions on Medical Imaging*, 22, 155–169.
- Malik, J., Belongie, S., Leung, T., & Shi, J. (2001). Contour and texture analysis for image segmentation. *International Journal of Computer Vision*, 43, 7–27.
- Maurer, C., Qi, R., & Raghavan, V. (2003). A linear time algorithm for computing exact euclidean distance transforms of binary images in arbitrary dimensions. *IEEE Transactions on Pattern Analysis and Machine Intelligence*, 25, 265–270.
- Moon, W., Lo, C., Chang, J., Huang, C., Chen, J., & Chang, R. (2013). Quantitative ultrasound analysis for classification of BI-RADS category 3 breast masses. *Journal of Digital Imaging*, 26, 1091–1098.
- Northacker, M., Duda, V., Hahn, M., Warm, M., Degenhardt, F., Madjar, H., et al. (2009). Early detection of breast cancer: Benefits and risks of supplemental breast ultrasound in asymptomatic women with mammographically dense breast tissue. a systematic review. *BMC Cancer*, 9, 335.
- Platt, J. (1999). Probabilistic outputs for support vector machines and comparisons to regularized likelihood methods. *Advances in Large Margin Classifiers*, 10, 6174.
- Rodrigues, R., Braz, R., Pereira, M., Moutinho, J., & Pinheiro, A. M. (2015). A two-step segmentation method for breast ultrasound masses based on multi-resolution analysis. *Ultrasound in Medicine & Biology*, 41, 1737–1748.
- Rouhi, R., Jafari, M., Kasaei, S., & Keshavarzian, P. (2015). Benign and malignant breast tumors classification based on region growing and CNN segmentation. *Expert Systems with Applications*, 42, 990–1002.
- Schulz-Wendtland, R., Fuchsberger, M., Wacker, T., & Hermann, K. P. (2009). Digital mammography: An update. *European Journal of Radiology*, 72, 258–265.
- Shan, J., Cheng, H. D., & Wang, Y. (2012). Completely automated segmentation approach for breast ultrasound images using multiple-domain features. *Ultrasound in Medicine & Biology*, 38, 262–275.
- Shi, J., & Malik, J. (2000). Normalized cuts and image segmentation. *IEEE Transactions on Pattern Analysis and Machine Intelligence*, 22, 888–905.
- Singh, B. K., Verma, K., & Thoke, A. S. (2016). Fuzzy cluster based neural network classifier for classifying breast tumors in ultrasound images. *Expert Systems with Applications*, 66, 114–123.
- Soh, L., & Tsatsoulis, C. (1999). Texture analysis of SAR sea ice imagery using gray level co-occurrence matrices. *IEEE Transactions on Geoscience and Remote Sensing*, 37, 780–795.
- Timmers, J. M. H., van Doorn-Nagtegaal, H. J., Verbeek, A. L. M., & den Heeten, G. J. (2012). A dedicated BI-RADS training programme: Effect on the inter-observer variation among screening radiologists. *European Journal of Radiology*, 81, 2184–2188.
- Valckx, F., & Thijssen, J. (1997). Characterization of echographic image texture by cooccurrence matrix parameters. *Ultrasound in Medicine and Biology*, 23, 559–571.
- Vapnik, V. (2000). *The nature of statistical learning theory*. New York, NY, USA: Springer-Verlag.
- Vedaldi, A., & Soatto, S. (2008). Quick shift and kernel methods for mode seeking. In *Proceedings of the European conf. computer vision* (pp. 705–718).
- Wang, W., Zhu, L., Qin, J., Chui, Y. P., Li, B. N., & Heng, P. A. (2014). Multiscale geodesic active contours for ultrasound image segmentation using speckle reducing anisotropic diffusion. *Optics and Lasers in Engineering*, 54, 105–116.
- Xi, X., Shi, H., Han, L., Wang, T., Ding, H. Y., Zhang, G., et al. (2017). Breast tumor segmentation with prior knowledge learning. *Neurocomputing*, 237, 145–157.
- Xian, M., Zhang, Y., & Cheng, H. D. (2015). Fully automatic segmentation of breast ultrasound images based on breast characteristics in space and frequency domains. *Pattern Recognition*, 48, 485–497.
- Xian, M., Zhang, Y., Cheng, H. D., Xu, F., Zhang, B., & Ding, J. (2018). Automatic breast ultrasound image segmentation: A survey. *Pattern Recognition*, 79, 340–355.
- Xie, Y., Chen, K., & Lin, J. (2017). An automatic localization algorithm for ultrasound breast tumors based on human visual mechanism. *Sensors*, 17, 1101.
- Yu, Y., & Acton, S. (2002). Speckle reducing anisotropic diffusion. *IEEE Transactions on Image Processing*, 11, 1260–1270.
- Zakeri, F. S., Behnam, H., & Ahmadinejad, N. (2012). Classification of benign and malignant breast masses based on shape and texture features in sonography images. *Journal of Medical Systems*, 36, 1621–1627.
- Zhang, D., Liu, Y., Yang, Y., Xu, M., Yan, Y., & Qin, Q. (2016). A region-based segmentation method for ultrasound images in HIFU therapy. *Medical Physics*, 43, 2975–2989.